Bachelor's thesis

NTNU
Norwegian University of Science and Technology
Faculty of Natural Sciences
Department of Materials Science and Engineering

Henrik Gobakken
Silje Li
Amund Ugelstad

Comparison of Electromagnetic Fields and Grain Refiners on Microstructure Evaluation of Al and Al-Si Alloys

Bachelor's thesis in Material Science & Engineering
Supervisor: Robert Fritzsch
May 2022

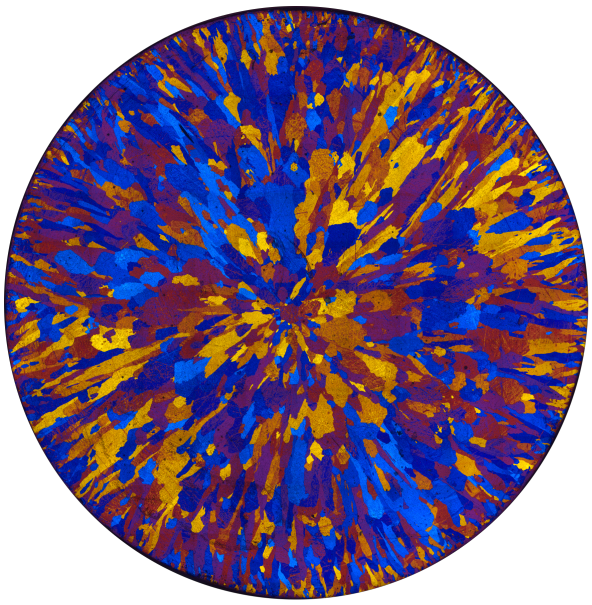

NTNU
Kunnskap for en bedre verden

Henrik Gobakken
Silje Li
Amund Ugelstad

Comparison of Electromagnetic Fields and Grain Refiners on Microstructure Evaluation of Al and Al-Si Alloys

Bachelor's thesis in Material Science & Engineering
Supervisor: Robert Fritzsch
May 2022

Norwegian University of Science and Technology
Faculty of Natural Sciences
Department of Materials Science and Engineering

NTNU
Norwegian University of
Science and Technology

NTNU
Norwegian University of
Science and Technology

Department of Material Science and Engineering

TMAK3001 - Bachelor in Material science

Comparison of Electromagnetic Fields and Grain Refiners on Microstructure Evaluation of Al and Al-Si Alloys

Sammenligning av effekten til elektromagnetiske felt og korn finere på mikrostruktur i Al og Al-Si legeringer

Authors:
Henrik Gobakken
Silje Li
Amund Ugelstad

Supervisor:
Prof. Robert Fritzsch

Spring, 2022

Summary of Graduate Project

Title:	Comparison of Electromagnetic Fields and Grain Refiners on Microstructure Evaluation of Al and Al-Si Alloys
Project no.	IMA-B-14-2022
Date:	20.05.2022
Authors:	Henrik Gobakken Silje Li Amund Ugelstad
Supervisor:	Prof. Robert Fritzsch
Employer:	Pyrotek, NTNU and Norsk Hydro ASA
Contact persons:	Amund Ugelstad 48265971 amundueland@gmail.com Henrik Gobakken 94195300 henrik.ross.gobakken@gmail.com Silje Li 90952307 00silje.li@gmail.com
Keywords:	Aluminium, Al-Si alloys, grain refiner, electromagnetic casting, micro structure
Pages:	50
Attachments:	5
Availability:	Open

Abstract:

The micro structure in aluminium can be altered by solidification rate, addition of grain refiners and electromagnetic stirring. Al 1370 and AlSi7 were cast with and without additions of three different titatium diboride grain refiners at four different solidification rates, as well as the alloys without grain refiner additions in four different electromagnetic field strengths. Results were gathered by grain size analysis and conductivity measurements. Addition of grain refiner, increasing solidification rate, and increasing magnetic field strength was found to reduce the grain size. Conductivity was found to have an inverse correlation with grain size.

Sammendrag av Bacheloroppgaven

Tittel:	Sammenligning av effekten til elektromagnetiske felt og korn finere på mikrostruktur i Al og Al-Si legeringer
Oppgave no.	IMA-B-14-2022
Dato:	20.05.2022
Deltagere:	Henrik Gobakken Silje Li Amund Ugelstad
Veileder:	Prof. Robert Fritzsch
Oppdragsgiver:	Pyrotek, NTNU og Norsk Hydro ASA
Kontaktpersoner:	Amund Ugelstad 48265971 amundueland@gmail.com Henrik Gobakken 94195300 henrik.ross.gobakken@gmail.com Silje Li 90952307 00silje.li@gmail.com
Nøkkelord:	Aluminium, Al-Si legeringer, korn finer, elektromagnetisk støping, mikrostruktur
Antall sider:	50
Antall vedlegg:	5
Tilgjengelighet:	Åpen

Sammendrag:	Mikrostruktur i aluminium kan påvirkes av størkningsrate, tilsats av kornfinere og røring ved bruk av magnetiske felt. Al 1370 og AlSi7 ble støpt med og uten tilsats av tre forskjellige titandiborid kornfinere og fire forskjellige størkningshastigheter, samt uten kornfiner i fire forskjellige elektromagnetiske feltstyrker. Resultater ble innsamlet gjennom analyse av kornstørrelse og konduktivitetsmålinger. Tilsats av kornfiner, økende størkningsrate og økende magnetisk felstyrke ble funnet å minke kornstørrelse. Konduktivitet ble funnet til å ha en invers korrelasjon med kornstørrelse.

Statutory Declaration

We declare that we have developed and written the enclosed thesis entirely by ourselves and in collaboration with the group signed onto this work, and have not used sources or means without declaration in the text. Any thoughts or quotations, which were inferred from these sources, are clearly marked as such.

This report was not submitted in the same or in a substantially similar version, not even partially, to any other authority to achieve an academic grading and was not published elsewhere.

Trondheim, May 2022	Henrik R. Gobakken	Silje Li	Amund Ugelstad

Preface

You are about to read "Comparison of Electromagnetic Fields and Grain Refiners on Microstructure Evaluation of Al and Al-Si Alloys". This thesis provides an experimental overview on how the grain size and distribution in commercially pure Al and AlSi7 is affected by solidification rate, electromagnetic fields and grain refiners. Furthermore, the thesis also contains an experimental part detailing casting procedure and analysis methods including conductivity measurements, polarized light microscopy and grain size analysis.

We had several reasons for choosing this as our bachelor thesis. We were intrigued by the opportunity to conduct pioneer level research in combination with relevant lab experiments. In addition, aluminium has been a central subject in previous assignments and lectures, and is an important material for Norway.

The thesis was written to fulfill the graduation requirements of a bachelor's degree in materials technology at The Norwegian University of Science and Technology (NTNU). We have been engaged in researching and writing this thesis from January to May 2022. Our scientific issue was formulated together with our main supervisor Dr. Robert Fritzsch. The research has presented challenges, but extensive work on the topic has yielded insight.

We would like to thank our main supervisor, Prof. Robert Fritzsch, for his time and expertise. His knowledge, insight, and experience were crucial for completing the bachelor thesis. We wish to thank the Department of Materials Science and Engineering, IMA, NTNU, for supporting our work financially, as well as all the technical staff at the same department, making it possible for us to solve problems as they arose. We would like to thank Norsk Hydro ASA and SINTEF for providing materials and Pyrotek for providing equipment. We also want to thank Hannes Zedel for supporting the project with with data analyses, and Lars Arnberg for helpful insights.

To our fellow students at NTNU - we would like to thank you for your wonderful cooperation, it was always helpful to discuss ideas and problems concerning our research with you.

Table of Contents

List of Figures

List of Tables

1 Introduction

1.1 Background

Aluminium has two main advantages over copper for use in high-voltage transmission lines. First, as aluminium is lighter than copper fewer pylons are required. Second, aluminium is significantly cheaper than copper per unit weight. Other properties such as mechanical strength and corrosion resistance makes aluminium a feasible option for high-voltage transmission lines.

Altering the grain size and distribution in a metal can change the mechanical properties of that metal, which is also true for aluminium. This can be done by changing the solidification rate, the addition of grain refiners and by the application of an electromagnetic (EM) field. It has been found in earlier studies (e.g. Metan 2009 [1] and Vives 1993 [2]) that the use of a strong EM field can influence the microstructure. While grain refiners can be used to adjust the microstructure, the addition of said grain refiners has been proven to influence the electrical conductivity of aluminium (e.g. Hassanabadi 2018 [3]).

1.2 Objective and experimental work

The objective of this study is to explore how solidification rate, the addition of grain refiner and the application of of an EM field affect the microstructure of commercially pure Al and Al-Si alloys. This includes how and to what extent the solidification rate, the addition of grain refiner, and the application of a magnetic field affects grain structure and electrical conductivity in these alloys. This exploration provides a base for further research into the use of EM fields for grain adjustment purposes and provides a comparison with the effects of solidification rate and grain refiners.

Commercially pure aluminium, hereby referred to as Al and the Al-Si alloy, AlSi7, supplied by SINTEF and three grain refiners supplied by Norsk Hydro ASA were used for the purposes of this experiment. These resources were used to cast 50 different samples for analysis. Three methods were used for casting. These three methods were repeated once for Al and once for AlSi7:

- The metal was melted then cast into four different moulds with varying solidification rate.
- Three different grain refiners were added to separate melts, before they were cast in the four moulds.
- Samples were cast in an EM field at four different strengths.

After casting, the samples were cut, polished to a flat surface, and then anodized. This was done to optimise imaging from polarised light microscopy of the prepared samples. These images were in turn analyzed by qualitative inspection and quantitative image analysis by deterministic segmentation. Though several more rounds of casting and an improved method are required to determine the optimal procedure for casting aluminium in an EM field, this work provides a base knowledge which highlights what variables affect the microstructure.

A systematic overview of the structure and main aspects of this thesis is provided in Figure 1

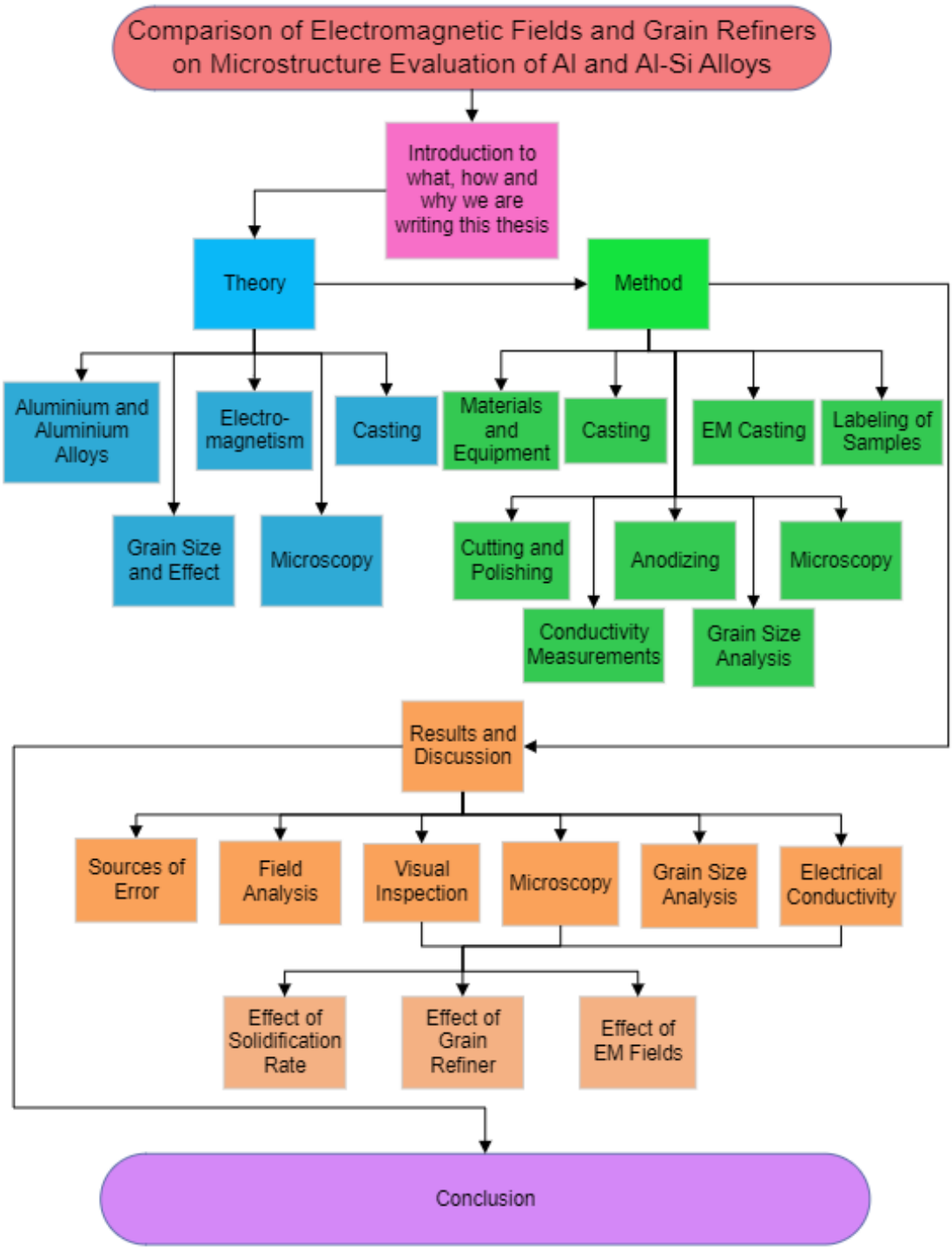

Figure 1: Flow chart of the thesis.

2 Theory

2.1 Aluminium and Aluminium Alloys

Aluminium is suitable for electrical purposes, as it is lightweight and considered a good conductor. By combining aluminium with other elements, new alloys can be customised to meet specific demands. Aluminium has a tensile strength between 186 and 510 MPa and a density of 2.7 g/cm^3, while stainless steel has a tensile strength between 515 and 1140 MPa and a density of 7.7 g/cm^3 [4]. The lower density allows aluminium to be used as an replacement for stainless steel under many circumstances. This versatility combined with its recyclability has made aluminium an important material for construction, aviation, transportation, and other sectors. The world is said to have entered the "age of aluminium", and the use of aluminium is expected to continue to increase.

Relevant properties for two commonly used alloys, commercial pure Al and AlSi7, are listed below in Table 1. The electrical conductivity of aluminium is altered substantially by impurities and defects. Alloying elements, such as silicon or magnesium, alter both thermal and electrical characteristics, while also affecting the physical properties of aluminium.

Table 1: Chemical composition in wt%, possible intermetallics [5], solidification temperature in °C [6] and electrical conductivity in %IACS for 99.7% Al and AlSi7 [4].

Alloy	Chemical composition [wt%]	Possible intermetallics	Solidification temperature [°C]	Electrical conductivity [%IACS]
Al 99.7%	Al 99.7 Fe 0.2 Si 0.1	$\beta - Al_5FeSi$, $\delta - Al_4FeSi$, $\alpha - Al_8Fe_2Si$	630 - 660	59.5 - 63.9
AlSi7	Al balance Si 6.5-7.5 Mg 0.4-0.7 Fe 0.15	$\beta - Al_5FeSi$, $\delta - Al_4FeSi$, $Al_9FeMg_3Si_5, Mg_2Si$ $\pi - Al_8Mg_3FeSi_6$	575 - 625	38.3 - 40.1

The electrical conductivity refers to a materials capability to conduct electric current. One common unit of measurement is the relative conductivity compared to the International Annealed Copper Standard(%IACS) [7]. The conductivity is determined by the type of atoms, and the mobility of electrons in a material. A material with weakly bound electrons can more easily move current due to higher electron mobility. In most metals the outermost electrons can be considered to be free due to their ability to move between adjacent atoms, resulting in a high electrical conductivity compared to non-metals. Aluminum is more conductive than silicon as silicon has more strongly bound electrons, restricting electric current [8] [4].

2.1.1 Magnetic Properties

A material which exclusively consists of paired electrons is diamagnetic, if unpaired electrons are present in the material, it is paramagnetic. For this reason, aluminium is paramagnetic, while for example aluminium oxide is diamagnetic. Both of which are considered non-magnetic because they do not exhibit magnetization unless being in the proximity of a magnetic field. In the presence of a magnetic field a paramagnetic material will align itself with the flux and a diamagnetic one will align itself perpendicular to the flux [9]. While being considered nonmagnetic, both commercial pure Al and AlSi7 are paramagnetic and will thereby exhibit weak attraction to magnetic fields.

The permeability, μ, measures obtained magnetization of a material in response to an applied magnetic field in H/m. Mathematically this is the ratio between the magnetic flux density, B, which is a measure of the actual magnetic field within a material and the magnetizing field, H. This relationship is shown in Equation 1.

$$\mu = \frac{B}{H} \tag{1}$$

The ratio between the permeability of the material, μ, and the permeability of free space, μ_0, gives the relative permeability, μ_r. This relationship defines the magnetization of a material and is shown in Equation 2.

$$\mu_r = \frac{\mu}{\mu_0} \tag{2}$$

μ_0 is approximately $4\pi * 10^{-7}$ H/m. If the relative permeability is less than one, the material is diamagnetic, whereas a relative permeability larger than one indicates a paramagnetic material [10]. The relative permeability of aluminium is slightly larger than one, thereby confirming that aluminium is paramagnetic. In comparison, the relative permeability of iron, which is a ferromagnetic material, is several thousands [4], depending on the purity of the material.

2.2 Electromagnetism

2.2.1 Electromagnetism and Inductors

Electromagnetism is the physical interaction between electrically charged particles. An inductor consists of a coil of conducting wire that induces a magnetic field when an electric current is passing through [11]. An inductor can have a solid or gaseous core, and are usually used to provide resistance to a DC current. The inductor is defined by its inductance L, which describes the physical parameters of the inductor. An illustration of a basic inductor is shown in Figure 2. Every turn in coil adds to the total sum of the magnetic field [12].

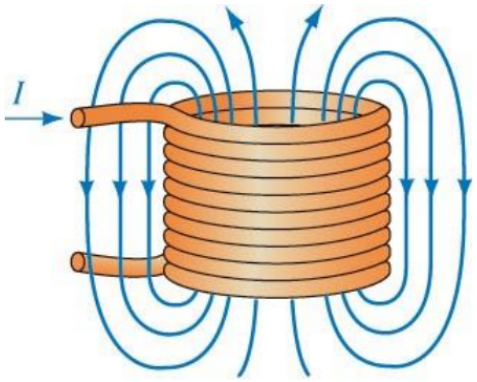

Figure 2: Illustration of a basic inductor in the shape of a round coil [13]. I is the electric current and the blue lines illustrates the magnetic field lines.

The magnetic field strength in the middle of the coil is inversely proportional to the cross-sectional area of the coil [14]. An inductor opposes sudden changes in current flowing through it. This means that an inductor meant to create a powerful switching magnetic field will experience a substantial increase in electrical resistance in the coil. Most large inductors are water-cooled to avoid excessive heating. [12].

Because of aluminium's conductivity, a changing magnetic field induces a current in the metal. The governing equations to describe this phenomenon are the Ampere's law with Maxwell's additions which expresses that magnetic fields either can be generated from electric current or by changing an electric field in a conductor. This makes it relevant for time-varying currents inducing time-varying magnetic fields. The other relevant equation is Faraday's law linking the changing magnetic field to the changes of the electric field [15].

The Ampere-Maxwell equation is shown in Equation 3:

$$\nabla \times H = J_f + \frac{\delta D}{\delta t} \tag{3}$$

where $\nabla\times$ is the curl operator, H is the the magnetic field, J_f is the conduction current density, D is the electric displacement field, and t is time [15]. Faraday's law of induction is mathematically described in Equation 4:

$$\Phi_B = \int\limits_{\sum(t)} \int B(t) * dA \tag{4}$$

where Φ_B is the magnetic flux for the surface $\sum(t)$, and $B * dA$ is the vector dot product which represents the element of flux through area dA [16].

The aluminium within the coils will experience changing electric fields as the alternating current (AC) generates varying flux. This induces Lorentz forces, which act as an electro-motive force on the metal. This force can be used to stir molten aluminium and achieve a more homogeneous temperature in the melt [17].

The Lorentz force law states that the electromagnetic force equals the cross product of induced current density and magnetic field strength, and is given in Equation 5:

$$F = qE + qv \times B \tag{5}$$

where F is the electromagnetic force on a particle with a charge q moving with velocity v through an electric field E and magnetic field B [18].

2.2.2 Skin Effect

Skin effect refers to the tendency of AC to avoid the centre of the conductor, and crowd on the surface. This reduces the cross-sectional area in which the current can flow, thus increasing the resistance of the conductor. By increasing frequency the skin effect is made more pronounced [19].

The skin effect can be visualized by the penetration depth of the magnetic field into different materials. The penetration depth defines how far the magnetic field can interact with the material in every cycle of the applied frequency. The conductivity is here the key parameter for paramagnetic and diamagnetic materials. Ferromagnetic materials also alter the penetration depth by the permeability. The equation for the electromagnetic penetration depth is shown in Equation 6:

$$\delta = \sqrt{\frac{\rho}{\pi f \mu_0 \mu_r}} = \sqrt{\frac{\rho}{\pi f \mu}} \tag{6}$$

where δ is the penetration depth in m, ρ is the electrical resistivity in Ω-m, f is the frequency in Hz, μ_0 is the permeability of free space, μ is the permeability of the material and μ_r is the relative permeability of the material [20].

From the equation it can be observed that the electromagnetic penetration depth is inversely proportional to the square root of the frequency. The electromagnetic penetration depth in mm as a function of frequency in Hz is plotted in Figure 3 for pure aluminium at 25 and 750 °C, as well as aluminium with high resistivity and A356 at 750°C. The Figure was provided by Prof. Robert Fritzsch.

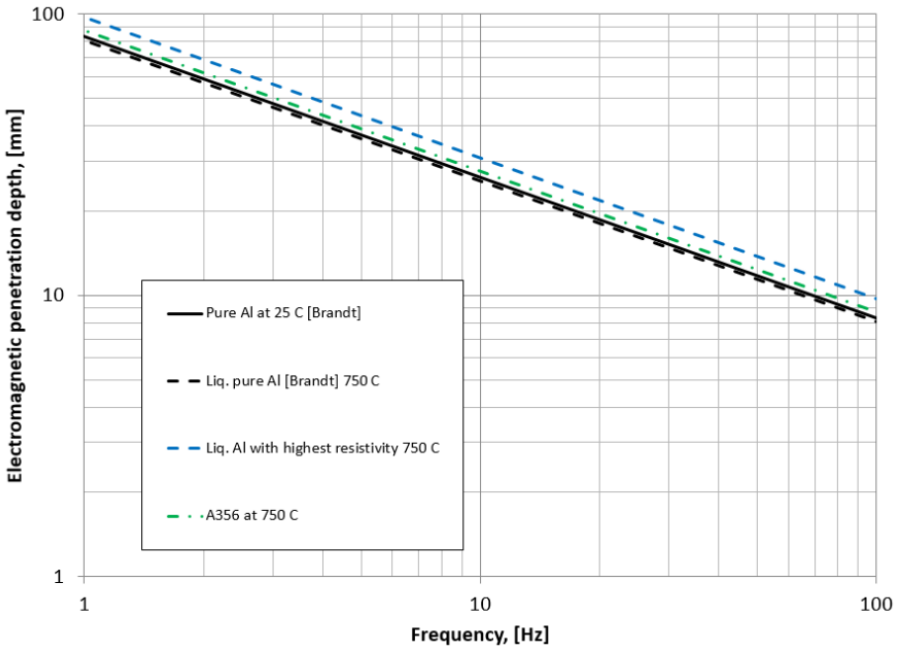

Figure 3: Electromagnetic penetration depth in mm as a function of frequency in Hz for aluminium at 25°C and 750°C (liquid), highest resistivity aluminium at 750°C (liquid) and A356 at 750°C(liquid).

2.3 Casting

Casting is the process of pouring molten metal into a prepared mould. The metal cools in the mould, inheriting its shape. Casting can be done with a variety of metals, like aluminium. Casting can make complex structures which could have been difficult to make with other manufacturing processes. However, casting can also result in a substandard microstructure causing the material to be brittle and have low strength. Machining the desired product from a solid block of aluminium takes time, while extrusion has a size constraint that casting does not [21].

The process of grain formation is illustrated in Figure 4. This figure shows how nucleation occurs and the grains grow resulting in irregularly shaped grain boundaries, illustrated as black lines. These irregular shapes can be hard to control and will contribute to the substandard microstructure often observed in castings. As these grains grow, impurities in the metal will start to concentrate in the remaining melt. This often results in a high concentration of intermetallics and impurities along grain boundaries, as these are the last areas to solidify.

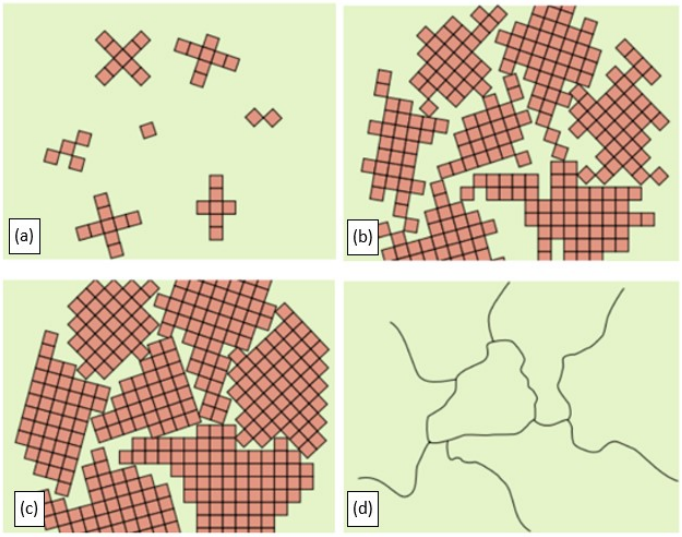

Figure 4: Illustration of grain and grain boundaries formation. (a) Nucleation starts, (b) the grains start to grow from nucleation sites, (c) grain boundaries form, (d) grain boundaries seen as black lines. [9].

2.3.1 Solidification Rate

Solidification is the process in which the atoms in a molten liquid are arranged into an ordered solid state. The solidification rate is the rate at which the molten liquid solidifies. The main factors that affects solidification rate is the temperature gradient and the thermal conductivity between the mould and the molten metal. A higher temperature gradient would lead to a faster solidification rate [21][22]. For solidification to instigate a nucleation point is needed. Nucleation requires a degree of undercooling or foreign particles introduced to the melt [23].

Chvorinov's rule is the mathematical expression for solidification rate and is given in Equation 7:

$$t = B\left(\frac{V}{A}\right)^2 \tag{7}$$

where t is the solidification time, V is the casting volume, A is the wall area of the mould, and B is the mould constant which is defined in Equation 8:

$$B = \left[\frac{\rho_m}{T_m} - T_0\right]^2 * \left[\frac{\pi}{4k\rho c}\right] * \left[L + c_m(T_pour - T_m)\right]^2 \tag{8}$$

where ρ_m is metals density, T_m is the metals solidification temperature, T_0 is the moulds initial temperature, k is the moulds thermal conductivity, ρ is the moulds density, c is the moulds specific heat, L is the metals latent heat of fusion, c_m is the metals specific heat, and T_{pour} is the metal pouring temperature [24].

While casting, the solidification rate is greatly reliant upon the material of the mould. This is due to the liquid phase having a higher energy than the solid phase. The solidification process is exothermic, meaning that the transition from a liquid to a solid releases' energy in the form of heat. A cast with high thermal conductivity will allow this energy to dissipate out of the system efficiently. A mould with a lower thermal conductivity will take longer to dissipate heat from the molten metal. This means that the molten metal retains more thermal energy for a longer time, decreasing the rate of solidification [21].

The shape and size of the mould affects the solidification rate. As shown in Figure 5 below, the solidification instigates along the edges and develops inwards. Thereby, the centre of the cast is

the last to solidify. Additionally, the mass of the mould influences the solidification rate. This is due to a larger mould requires more energy than a smaller one before heating up to the same temperature. Thereby keeping the temperature gradient lower, thus increasing the solidification rate of the molten metal [21].

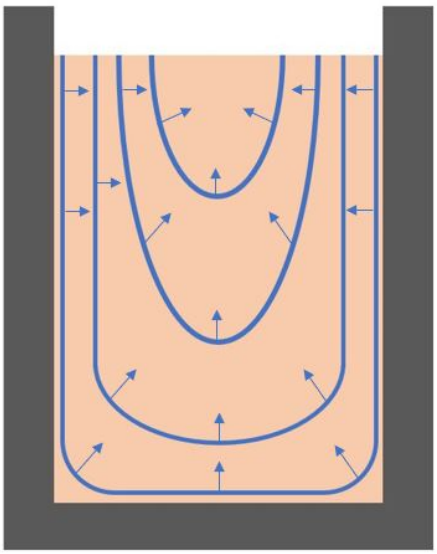

Figure 5: Solidification of molten aluminium in a cylindrical mould from the mould walls.

Figure 6 shows the phase diagram of a binary Al-Si system. This diagram explains how AlSi7 with 7 wt% Si will start to solidify at around 630 °C. The first phase to solidify will be α-Al, which makes the concentration of Si in the remaining melt increase. The difference in solidification temperature between α-Al and Al+Si Eutectic is around 50 °C. This causes a lot of small α-Al particles to nucleate and move around while the Al-Si is still liquid and growing on α-Al. This leads to a smaller grain size and a more uniform distribution of grains.

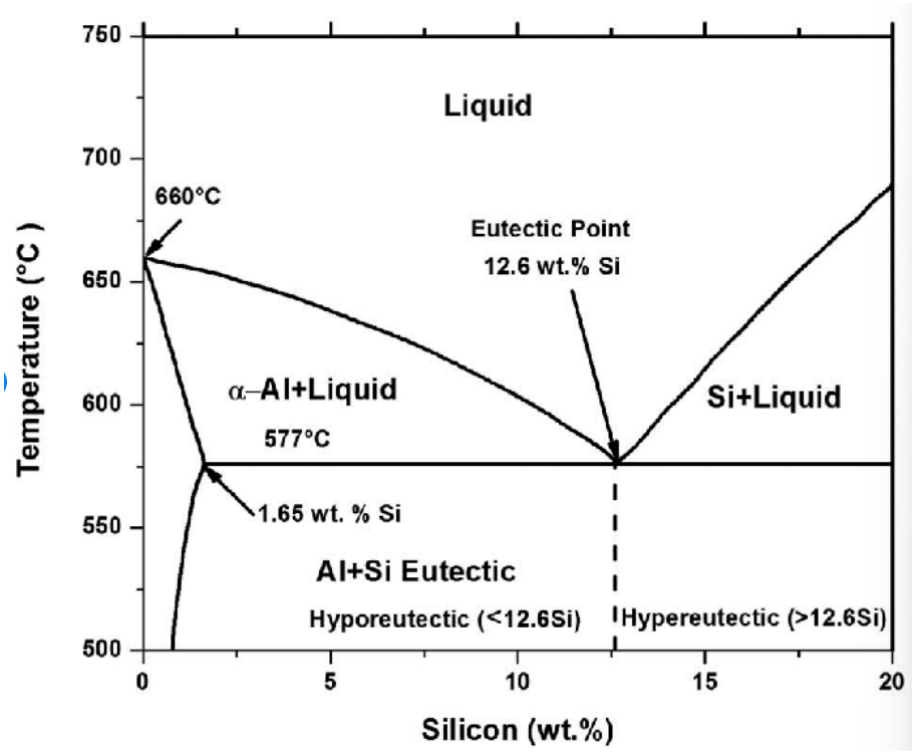

Figure 6: Phase diagram of aluminium with wt% silicon [6].

2.3.2 Shrinkage and Pores

Solid aluminium has FCC structure, which has the densest packing fraction of 0.74 [9]. When aluminium solidifies, a substantial and rapid volume change occurs as it changes from the less dense packing of liquid aluminium to the denser FCC structure. Liquid aluminium at 700 °C has a density of 2368 kg/m^3, while solid aluminium at 600 °C has a density of 2550 kg/m^3. The volume change for aluminium as it solidifies is therefore 7.14%. As the solid aluminium cools down further from 600 °C to 25 °C it shrinks another 5.1% and has a density of around 2700 kg/m^3 [25]. This effect can be observed as a reduction in solid aluminium volume compared to the volume inside the mold. This reduction in volume is typically seen as a dimple on top of the cast, which is formed when the still molten metal moves down to replace the reduced volume of solid aluminium [26]. This shrinkage can also lead to shrinkage pores, where different parts of the cast either solidifies or shrinks at different times, creating a porous area inside the cast [27]. A typical shrinkage pore is exemplified in Figure 8 (a).

Molten aluminium reacts with moisture in the air to create aluminium oxide and hydrogen that dissolves into the metal [28]. The solubility of hydrogen in aluminium is shown in Figure 7. This plot shows that the hydrogen solubility increases with temperature, and increases drastically when the metal changes from solid to molten.

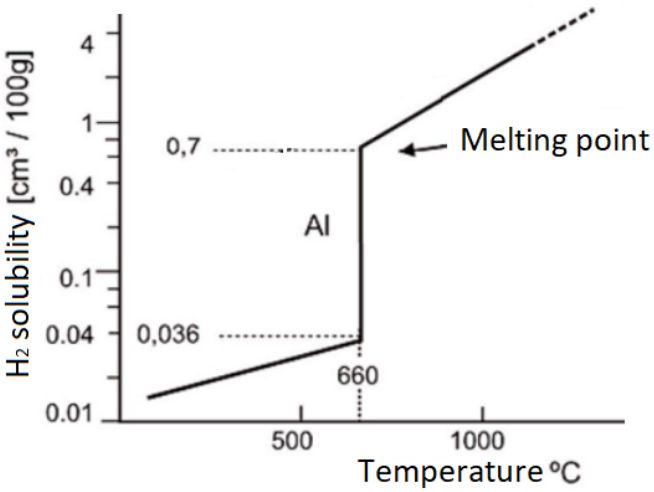

Figure 7: Solubility of hydrogen in aluminium as a function of temperature [28]

The dissolved hydrogen in molten aluminium will recombine to form (H_2) gas and reach an equilibrium concentration in the metal depending on the relative humidity in the air and the temperature. When the aluminium is cast and starts to cool down and solidify, most of the dissolved hydrogen will recombine to form H_2 gas [29]. This will create small gas bubbles that nucleate at impurities or grain boundaries in the melt. Dissolved hydrogen around these bubble will mostly add to the gas volume instead of creating a new nucleation point. These gas bubbles may then be trapped in the melt and create a gas pore as shown in Figure 8 (b) [30].

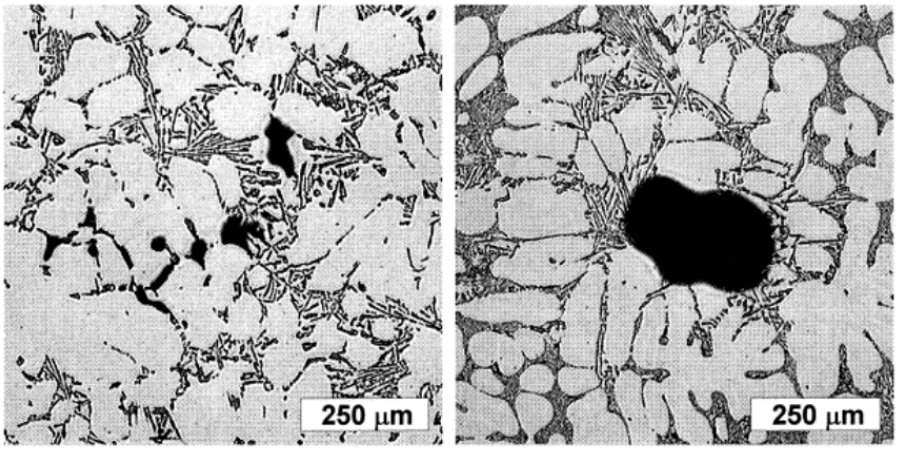

Figure 8: Cast aluminium alloy with (a) a typical shrinkage pore and (b) a typical gas pore [31].

Both shrinkage pores and gas pores are undesirable in cast metal, as they will affect the metals properties negatively. Aluminium is especially prone to gas pores because of its ability to dissolve high amounts of hydrogen and is usually degassed before being cast. [32]

2.3.3 Dendrites

In metallurgy, a dendrite is a tree-like structure of crystals growing as the molten metal solidifies. The shape seen in a scanning electron microscope (SEM), shown in Figure 9, is produced due to

growth being more energetically favourable in certain crystallographic directions. The growth of these dendrites affects the material properties.

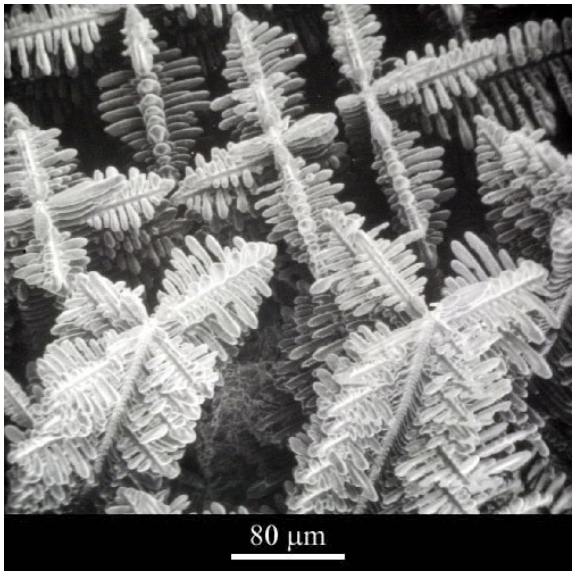

Figure 9: A SEM image of dendrites in a cobalt-samarium-copper alloy [33].

In order to attain dendrites, the given metal has to be undercooled below the freezing point of the metal. During casting of aluminium, the temperature decline is generally rapid enough to cause undercooling and thereby promote dendritic growth. The growth rate of the crystalline solid is largely dependent on the dispersion of heat away from the material. The nucleation and growth will determine the size of the grains, while proximity to adjacent dendrites determines the spacing. A slow cooling process would result in less nucleations compared to a rapid cooling process. This growth will result in dendrites of larger size [33]. Dendritic growth is also more prominent in samples with a larger solidification range. Al has a smaller solidification range than alloys such as AlSi7.

2.3.4 Electromagnetic Casting

Electromagnetic casting (EMC) is the process of subjecting molten aluminium to a magnetic field while it solidifies. This process can be used to solidify aluminium without contact with the cast, thereby creating a smooth surface. It can also be used to influence properties of the metal, such as grain size. Other than using EM fields to stir the aluminium and achieve a more homogeneous temperature [17], it can be used to increase the amount of nucleation points in the melt without adding grain refiners. As a result of the skin effect, which is explained in 2.2.2 Skin Effect, the electric current moves along the edges of the conductor. When current passes through a material with thin dendrite structures, the current will move along the edges of the dendrites. This induces a magnetic field in each dendrite branch that could break them apart. These pieces of loose dendrites can then move around in the melt and act as seeds or nucleation points and increase the amount of grains in the cast.

Because of the stirring caused by most EM-fields the metal experiences, the molten metal will move in a very turbulent way. When H_2 bubbles starts to form in molten aluminium as explained in 2.3.1 Solidification Rate, this turbulent motion traps more of the bubbles in the melt. This increases the volume of gas porosity in the cast.

2.4 Grain Size and Effect

Aluminium normally solidifies in a polycrystalline state, where the metal consists of several smaller crystals often referred to as grains. These grains are oriented in different directions and the size can vary a lot depending on how the sample is made. Figure 10 shows how grains can be distributed in a metal, where each colour is a grain oriented in a different direction.

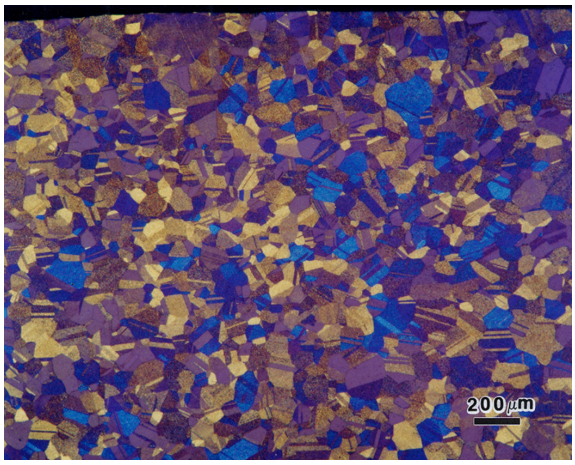

Figure 10: An example of grain size distribution in gold metal [34].

Properties of aluminium are greatly affected by the grain size in the metal. This makes grain size refinement an important part of casting or manufacturing parts in aluminium. One important property affected by grain size is the yield strength of the material. Yield strength is defined as the stress at which a material begins to experience plastic deformation. The relationship between grain size and yield strength is described by the Hall-Petch equation [9]:

$$\sigma_y = \sigma_0 + \frac{k_y}{\sqrt{d}} \tag{9}$$

where σ_y is the yield strength, σ_0 is a materials constant for starting stress for dislocation movement, k_y is a strengthening coefficient unique to each material and d is the average grain diameter. This relationship shows that as the grain size decreases, the yield strength can increase substantially. This is because plastic deformation mainly happens by moving dislocations, and grain boundaries act as pinning points that impede further propagation of these dislocations. Therefore, as the number of grains and grain boundaries increase, the yield strength also increases [9].

2.4.1 Microstructure Effect on Conductivity

The overall electrical conductivity of a metal sample is mostly determined by its the least conductive area, which is usually the poor conductivity at grain boundaries. Somewhat counter-intuitively this means that samples with large grains and few grain boundaries are expected to have a lower conductivity compared to samples with smaller grains. This is because fewer grain boundaries leads to a higher concentration of intermetallics and impurities in these boundaries. These often have a very low electrical conductivity compared to metal grains and lowers the already poor conductivity at grain boundaries even more. This leads to a considerable drop in overall electrical conductivity in samples with large grains [35][36].

2.4.2 Grain Refiners

The first aspect of the solidification process is nucleation, the spontaneous forming of small solid nuclei in the liquid mass. Places where the liquid metal is in contact with a foreign material are

optimal for nucleation. The edges of the mould or oxide particles or impurities are such places [37].

Certain particles, such as TiB_2, can act as grain refiners in very small percentages. The grain refiners stay solid in the molten aluminium, thereby acting as nucleation points. This increases the amount of grains that starts to grow, leading to a reduced grain size. While grain refiners offer the advantage of smaller grains, they also come with some disadvantages. The grain refiner may pile up in certain areas creating a less homogeneous material [37]. It also adds an artificial contamination to the metal.

$AlTi_5B_1$ and $AlTi_3B_1$ are common grain refiners with varying contents. $AlTi_5B_1$ and $AlTi_3B_1$ are aluminium samples with 5 wt% and 3 wt% titanium respectively, and 1 wt% boron. This means that the grain refiners contain some amount of pure elements, as well as TiB_2 particles. All samples have parts of other foreign elements, most notably iron, silicon, vanadium and potassium. Titanium has a melting point at 1668°C and boron at 2076°C, these materials will therefore not melt during the casting [4] and may act as nucleation points. TiB_2 particles agglomerate at high temperatures, it is therefore not ideal to leave grain refiners in molten metal for a longer time than necessary before casting. The temperature of the aluminium with grain refiners should exceed 750°C as the morphology will change into dendritic structure [38].

The quality of the grain refiner is dependent on many factors, and it is therefore possible to gain different effects from grain refiners with similar composition. An example of this is the $AlTi_3B_1$ grain refiner from the different producers KBM and GR, which therefore can have different abilities even though they have the similar content.

2.5 Microscopy

2.5.1 Polarized Light Microscopy

Polarized light microscopy (PLM) is a contrast enhancing technique that can be used to study a wide range of anisotropic specimen. PLM achieves a high level of contrast in these specimens from the interference created between horizontal- and vertically polarized light reflected from the sample. Aluminium grains are isotropic. To achieve contrast between different grain orientations, aluminium must first be anodized in a solution such as Baker's reagent. This creates an anisotropic alumina layer that is ordered depending on the orientation of the grain and makes it possible to study the grain size in aluminium samples [39][40].

2.5.2 Scanning Electron Microscope

A scanning electron microscope (SEM) scans a focused beam of high-energy electrons across a sample surface. A detector then picks up different signals that are created when the electrons hit the sample to generate an image of the surface. The most common signals used to create images in a SEM is secondary and backscattered electrons. A main advantage of SEM is that these electrons can be used to gather information of not only topography, but also chemical composition in the sample. The resolution is also substantially greater compared to traditional light microscopy, and can usually reach magnification greater than 25 000X [41]. Most SEMs are capable of energy dispersive x-ray spectroscopy (EDS). This is a technique that can be used to determine specific elements that make up different areas of a sample. The biggest limitation for EDS is that relatively light atoms like boron can not be detected. [42]

3 Materials and Methods

An overall representation of the steps in the methods is given in Figure 11. The blue represent casting processes, orange - sample preparation, and green - analysis. More detailed descriptions of the procedures are given below.

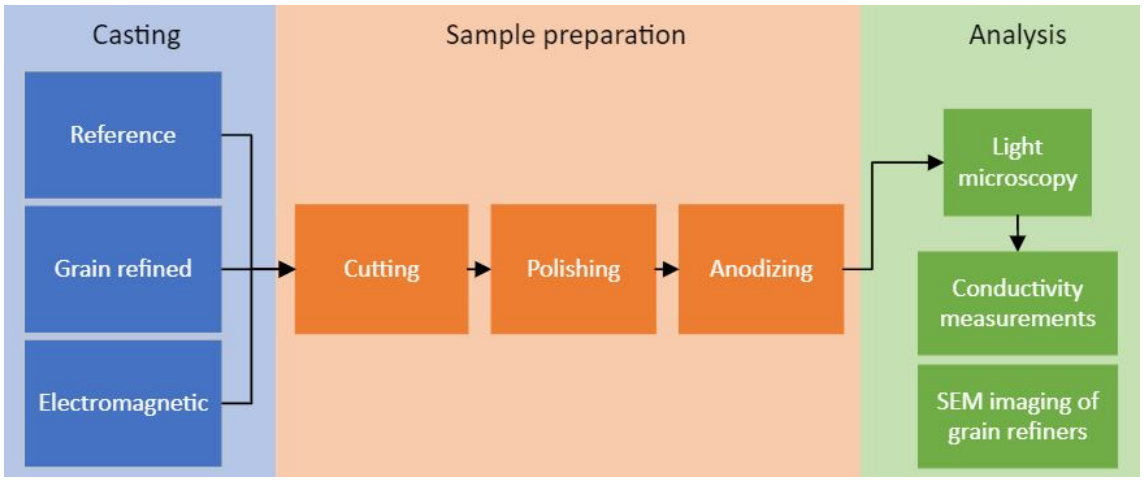

Figure 11: Flow chart of the methods starting from the left.

3.1 Materials and Equipment

The following materials and equipment were used in the experiments. The equipment is grouped under casting, electromagnetic casting, cutting and polishing, and etching and microscopy to clarify where they were used. In addition to the equipment listed below appropriate HSE gear was used.

Materials:

- Commercial pure Al of 1370 series (Al 99.7%)
- AlSi7 (Si 6.5-7.5%, Mg 0.4-0.7%, Al balance)
- Grain refiners:
  1. KMB $AlTi_3B_1$
  2. GR $AlTi_3B_1$
  3. Aleastur $AlTi_5B_1$

Casting:

- Cylindrical iron mould
- RSD iron mould
- Graphite mould
- Crucible
- Insulated cover with lid for graphite mould
- Furnace
- Thermometer connected to thermocouple
- Insulated cover plate
- Casting tools

Electromagnetic casting:

- Coil made of insulated copper tubing
- 5180 Gauss/Tesla meter
- Chauvin Arnoux F407 power harmonics meter
- Transformer for low field
- Variac variable transformer
- Transformer for high field

Cutting and polishing:

- Labotom-5 cutting machine
- 20A25 cutting blade
- EpoFix resin
- Saphir 550
- Diamond fluid 15 and 3 µm
- 320 grit sand paper
- Largan 9 polishing plate
- Allegard 3 polishing plate
- Utrasonic bath with isopropanol
- Ethanol

Etching and microscopy:

- Bakers reactant (10 ml 48% HBF_4 to 400 ml H_20)
- DC power supply
- Light microscope with polarizing filter
- SEM

Conductivity measurments:

- Electrical conductivity meter (AutoSigma 3000)

3.2 Casting

One kilogram of molten metal was heated to 730 °C ± 10 °C. The metal was melted in a graphite crucible coated with boron nitride (BN). After melting the metal, the dross was removed using a graphite rod. Two graphite moulds were pre-heated, one to 250°C, and the other to 650°C and placed in an insulted refractory cover. This was done to ensure that the solidification rates in the different moulds are optimal for analysing the effect of solidification rate on the grain size. The cylindrical iron mould and rapid solidified disc (RSD) iron mould were kept at room temperature. The moulds can be seen in Figure 12. The dimensions of the casting moulds as well as the insulation are given in Appendix A.

After ensuring that the molten metal was in correct temperature range and removing the dross, the metal was poured into the moulds. For samples with grain refiner, 0.1 wt% of grain refiner was added when the metal reached a temperature of 730 °C ± 10 °C. The melt was then stirred with a graphite rod for 30 seconds prior to pouring into the moulds. The procedure was executed in the same manner for Al, AlSi7, both with and without the KBM $AlTi_3B_1$, GR $AlTi_3B_1$ and $AlTi_5B_1$ additions. This resulted in 32 regular casting samples. Al without grain refiner was cast an additional time in both graphite molds.

Figure 12: Left to right: cylindrical iron mould, RSD iron mould, heated graphite mould at 250°C and insulated heated graphite mould at 650°C.

The four different moulds were used to achieve different solidification rates whereas the solidification rate reduces from fastest to slowest from left to right for the moulds in Figure 12.

3.3 Electromagnetic Casting

The method of EMC applies an electromagnetic field during the casting process. A F407 power harmonics meter and a 5180 Gauss/Tesla Meter was used to measure and calculate voltage, current, real power, apparent power and field strength for the EM fields. These measurements were taken at the edge and center at the top, middle and bottom of the mould in the EM fields. These results were used to model the EM fields in COMSOL. The following methods were used for the two different setups for EMC.

3.3.1 Pancake Coil

Aluminium was melted as described above and a graphite mould was heated to 750°C and placed in an insulated cover. This ensured that the metal did not begin to solidify before the coil was placed around the cast and the magnetic field could be induced.

The liquid metal was poured into the mould as fast as practically possible, the lid was placed on top, and the top of the coil was moved over the mould. The coil was connected to a step down transformer, driven by a high current VariAC, which was used at three different voltage outputs, giving three different field strengths. All fields were generated using mains frequency of 50 Hz. The cast was kept in the field for 10 minutes, until the metal solidified. The procedure was executed for Al and AlSi7, twice for each voltage and alloy, resulting in 12 samples from the pancake coil. The power at these three different voltages is shown in Table 2 and the average field strength was calculated from the measurements detailed in Appendix B.

Table 2: Voltage, current, real power, apparent power and average field strength for the three different field strengths.

Field	Voltage [V]	Current [A]	Real power[W]	Apparent power[VA]	Average field strength[mT]
α	1.33	76	90	101	2.20
β	2.76	154	380	427	4.20
γ	4.05	226	816	915	6.04

The coil and how the mould was placed in the coil are shown in Figure 13. An insulated plate was placed on the bottom part of the coil to ensure that possible aluminium spill did not get in contact with the coil. The dimensions of the coils are given in Appendix C.

Figure 13: Pancake coil and an insulated graphite mould at 750°C placed in the coil.

3.3.2 Round Coil

Aluminium was melted, as described above, and a graphite mould was heated to 750°C and placed in an insulated cover. The aluminium was poured in the mould and a lid was placed on top. The

water cooled coil was then placed around the mould as shown in Figure 14 and the magnetic field was then induces. The dimensions of the coil are given in Appendix C.

Figure 14: Insulated graphite mould heated to 750°C placed in the round coil.

The coil was driven directly from a step down transformer, controlled by a switch. The cast was kept in this position for 20 minutes, until the aluminium solidified. This process was repeated twice for both commercially pure Al and AlSi7, resulting in 4 samples from the round coil cast. The coil was kept at the same power for all casts, the power is given in Table 3 and the average field strength was calculated from the measurements detailed in Appendix B.

Table 3: Voltage, current, real power, apparent power and average field strength for the round coil casting.

Voltage [V]	Current [A]	Real power [W]	Apparent power [VA]	Average field strength [mT]
28	738	11 500	20 600	158.56

3.4 Labelling of Samples

An overview of which moulds were used for the different casts as well as labelling of the samples are shown in Table 4.

Table 4: Labelling, casting type, type of mould, temperature of mould and number of samples.

Sample label	Casting type	Mould used	Temperature	Number of samples
A	regular	Cylindrical iron mould	-	8
B	regular	RSD iron mould	-	8
C	regular	graphite mould	250°C	9
D	regular	insulated graphite mould	650°C	9
P	EMC pancake coil	insulated graphite mould	750°C	12
R	EMC round coil	insulated graphite mould	750°C	4
-	Grain refiner	-	-	3

Further in the report the samples are referred to by their alloy, Al or AlSi7, and their representative letter as described in Table 4. The samples with grain refiner added are also labelled with 1 if there is addition of KBM $AlTi_3B_1$, 2 for GR $AlTi_3B_1$ addition and 3 for Aleastur $AlTi_5B_1$ addition.

For example, a sample of AlSi7 and KBM AlTi3B1 grain refiner from the A mould is labelled AlSi7-1-A. Samples of the pancake coil are labelled with their field strength, α, β or γ as described in Table 2, and a P for pancake coil. Rectangular cross section samples are labelled with an X at the end.

3.5 Cutting and Polishing

All A samples were cut 27-31 mm above the bottom. All B samples were cast in Epofix resin. Around 5 mm was then cut off from the bottom of the sample. The remaining half of the sample was left encased in resin to later be polished. How the A and B samples were cut are shown in Figure 15. One sample from each of the different EMC samples, as well as the additional Al-C and Al-D were cut into rectangular cross section. The samples were cut 17-24 mm above the bottom of the sample as shown in Figure 16.
The samples were polished with a Saphir 550 shown in Figure 17, in the following order: Aluminium oxide P500 grit sandpaper until plane, 15 µm diamond particle solution on Largan 9 plate for five minutes, 3 µm diamond particle solution on Allegard 3 plate for five minutes and then OP-S on a cloth disc for five minutes. Between each paper switch the samples were rinsed in water. Before the diamond and OP-S polishing, the samples were rinsed in ethanol and an ultrasonic bath for two minutes.

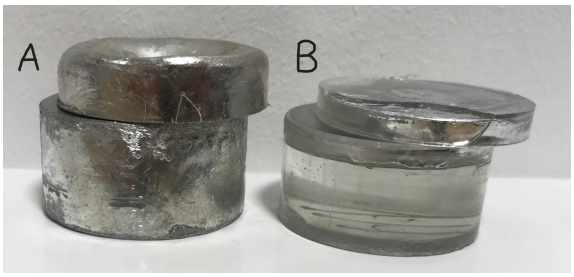

Figure 15: Cut of A and B samples.

Figure 16: Rectangular and circular cross section of the C, D, P and R samples.

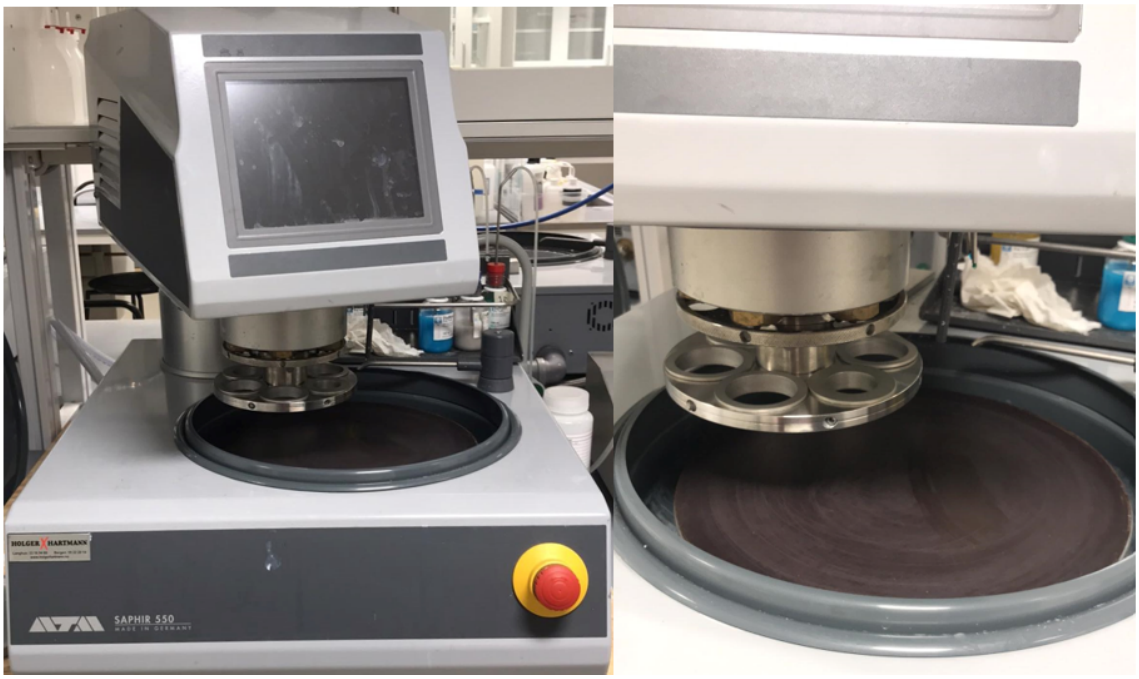

Figure 17: Saphir 550 polishing machine and the sample holder on the machine.

3.6 Anodizing

A Bakers reactant bath was connected to the negative pole of a DC power supply at 3 amps and 20V. The sample was held with the polished side down in the liquid, with a platinum thread connected to the positive pole held onto the backside of the sample. The sample was held like this for 2-4 minutes. The anodizing time varied for some samples, these were done in increments of 30 seconds after 2 minutes until a good contrast was seen in the microscope. The samples were scrubbed with soap and cotton and then rinsed with ethanol directly after anodizing. The setup is shown in Figure 18.

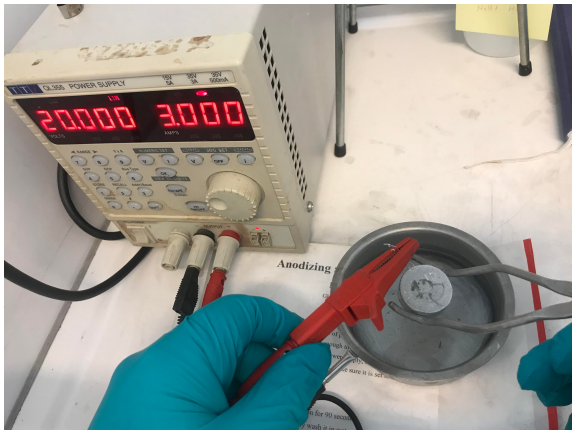

Figure 18: Setup for anodizing samples.

3.7 Microscopy

The samples were examined using an Univar microscope equipped with an automatic stage, polarized light capabilities and 15X magnification, shown in Figure 19 (left). This is a top-down microscope, which made it necessary to use a sample holder to keep the specimen parallel to the

stage. Each sample was captured completely by using the automated stage to cover the entire surface while capturing photos. The stage captured photos in lines from left to right, top to bottom, as illustrated in Figure 19 (right). The photos were then stitched together to create an image of the entire sample surface. This was all done using Image-Pro® Plus and Stage-Pro® software.

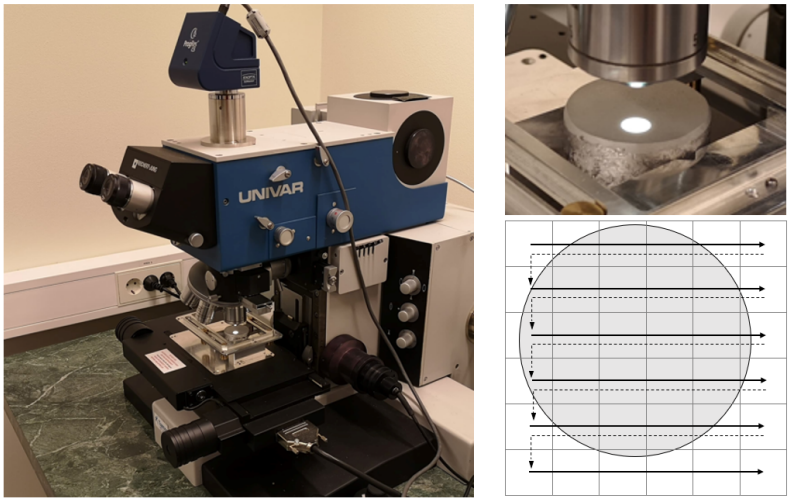

Figure 19: Overview of how the microscope and each sample was set up (left) and how the automatic stage moved across each sample (right).

Samples of the pure grain refiners were examined in a SEM using an SE2 detector and an acceleration voltage of 15kV.

3.8 Conductivity Measurements

As part of the justification of this experiment was to maintain electrical conductivity in aluminium, while reducing grain size, it is prudent to measure said conductivity. An electrical conductivity meter which is shown in Figure 21 was used to measure the conductivity of the material. The meter was first set to 500 kHz and calibrated. All Al samples were then measured, before the process was conducted again for the AlSi7 samples. The conductivity of each sample was measured 3 times. First at one edge, then at the centre before the last measurement was taken at the edge opposite of the initial measurement, as shown in Figure 20.

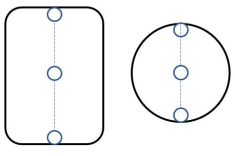

Figure 20: The positioning of the conductivity measurements across the rectangular and the circular samples.

Figure 21: Conductivity meter.

3.9 Grain Size Analysis

The images gathered from SEM for the grain refiner samples and light microscopy for the refined metal samples were analysed. This included observing grain size, orientation and growth patterns, as well as porosity. In addition to the visual inspection, as in called qualitative observations, the samples were analysed using a custom-made grain analysing algorithm, yielding quantitative results.

The algorithm organizes the grains based on size, given in equivalent spherical diameter (ESD) and the count of the grains in different size ranges. This data is structured in the diagram in Figure 22. The top left picture in the figure is the original microscope picture and the top right is how the program divides the RGB image into different color classes using k-means clustering. The center picture in the figure is a list of the different phases and their area of the sample, ESD range and mean ESD. The surface area of the sample and average grain size is also given.

There are some inaccuracies to this process because adjacent grains are identified as larger agglomerates rather than individual grains. Holes and pores are also counted as grains, but have been removed from the calculations as they show up as separate phases. The same method is used for all samples, and the results are perceived as sufficient for a comparison for the samples with larger grains.

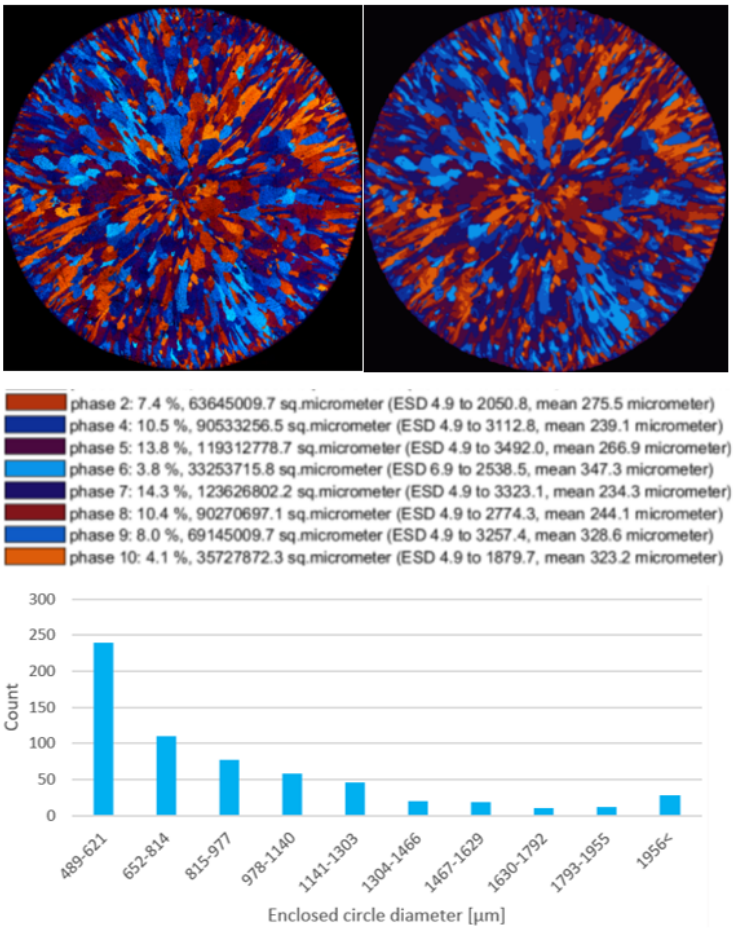

Figure 22: Information given from grain size analysis.

4 Results and Discussion

4.1 Sources of Error During the Experimental Execution

Due to the experimental procedure consisting of multiple processes, several sources of errors need to be addressed. The most prominent of these are listed below and further discussed.

- Pores and holes in the samples.
- Inconsistencies in time, temperature and mass during casting.
- Inconsistencies in the height at which the samples were cut and examined.
- Scratches on the sample surface.

4.1.1 Casting

As the samples were cast manually, we experienced inconsistencies in the mass of the sample. The time between taking the crucible out of the oven and the metal being poured into each mould and the temperature of the aluminium and moulds varied slightly between each round of casting. While the same moulds were used throughout the experiment, some samples may have been over or under filled, altering the amount of metal in the same samples from separate batches. In turn, a sample with more metal could extend the time needed for solidification as it would hold more thermal energy due to its larger mass. During casting, the same procedure was maintained for each mould, however slight time variations are likely to have occurred. These time variations made it so the aluminium cooled down to different temperatures while still in the crucible. This temperature difference added to the 20 °C difference in the casting temperature of the aluminium set at 730 °C $\pm$ 10 °C, resulting in a total difference that slightly varies solidification times between the samples.

During EM casting, the field had a noticeable effect on the protective steel layer on the floor, causing it to vibrate and possibly shake the sample as it solidified. The experimental setup was placed on a pallet in order to increase the distance between the coil and steel layer and somewhat reduce these vibrations. The movement of the metal floor may still have caused additional stirring which could alter the intended effect of the magnetic stirring. The vibrations were most prominent during the round coil casts, likely due to the stronger magnetic field. This could have been avoided by exchanging the metal sheet for a non-metallic flooring capable of withstanding molten aluminium spills.

4.1.2 Cutting and Polishing

Inconsistencies of the cutting height are to be expected, as well as variable angles since a ductile cutting blade was used. The samples may have been polished so that more than one plane appear on the surface of the sample. There were observed scratches on the sample surface during polishing which likely came from small particles which loosened from the surface. Due to how soft aluminium is, some aluminium oxide-particles from the sandpaper were embedded into the sample surface during polishing and may have caused scratches to form if they were released from the sample at a finer polishing stage.

4.1.3 Anodising and Microscopy

During anodising, the voltage was kept constant, but the samples drew more current depending on their surface area. Larger area resulted in higher electric current. This caused the 3 amp limit of the power supply to be reached, and the voltage had to be reduced to 10V for around 15 seconds, and then raised back up to 20V. The distance the sample was held from the bottom of the Baker's reagent bath also influences the effect of the process. In addition, hydrogen gas developed on the sample surface and gathered as bubbles on the surface, reducing the contact area between the sample and the solution. Although the samples were cleaned after anodising, a small amount of

Baker's reagent was trapped in narrow pores in some samples. This caused deterioration of the sample surface after anodising.

4.1.4 Conductivity Measurements

The results acquired from the conductivity meter, reliant on the state of the sample and the accuracy of the meter. Several samples had substantial defects and markings from casting and anodising, that would affect conductivity. Some of the samples also had a slight coating of deposited silica from OP-S or other materials causing disruptions in the measurements. The meter itself was also found to change measurement values with time passed from last calibration. This was corrected by measuring the first sample again after all samples were measured. This measurement was then compared to the first measurement of the sample. From this, a linear drift was assumed and the results for the other samples were corrected with this value. The drift may have been caused by a temperature difference in the probe or the samples, as conductivity is dependent on temperature [43].

4.2 Field Analysis

The different field strengths are given in Table 2 for the pancake coil and Table 3 for the round coil. To summarise, the average strength in mT is 2.20 for αP, 4.20 for βP, 6.04 for γP, and 158.56 for R. From these values it is clear that the strength span internally in the P field are remarkably lower compared to the R field.

The P and R coils have different magnetic fields due to their differences in shape and will therefore have different effects on the liquid aluminium. These coils were simulated in COMSOL Multiphysics® to get a better understanding of how the magnetic field penetrates the metal and affects it. These models were provided by Prof. Robert Fritzsch. The γP field is shown Figure 23. The simulated properties of the magnetic field match our measured values well enough to assume that the simulated velocities are close to reality.

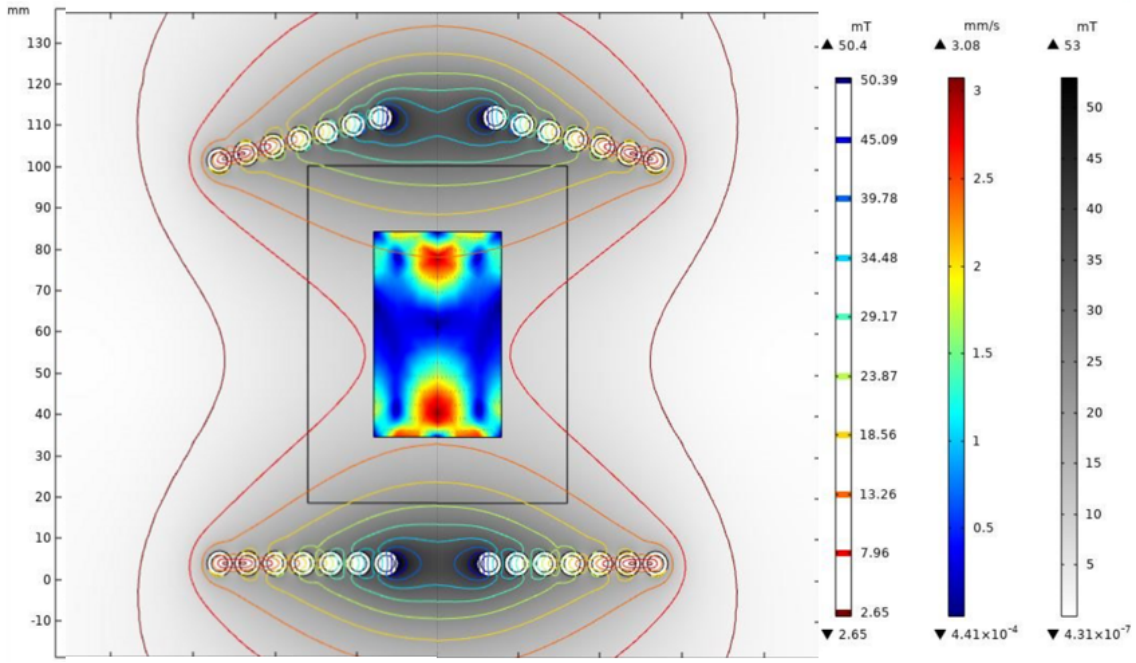

Figure 23: Comsol model of the γP field with magnetic strength and flowrate of liquid Al.

The movement of the liquid aluminium in the γP EM field is given in Figure 24. Here the red arrows indicates the direction of the movement and the colour the speed which is the same as in Figure 23. From the figure it can be observed that the liquid metal moves from the sides to the center of the sample.
The model of the round coil (R) field is shown in 25. The red arrows indicate the direction of movement in the liquid metal. The direction of movement are similar for both the P and R field, but the R field has a higher field strength resulting in more movement.
The inductive heat added to the metal is approximately 400 to 1200 W for the R field and and below 10 W for the P fields [44]. For the R field this value is high enough to drastically increase how long it takes for the sample to solidify. For the P field, this value is a minuscule amount compared to how much heat energy is already in the metal and is not likely to affect the time it takes for the sample to solidify.

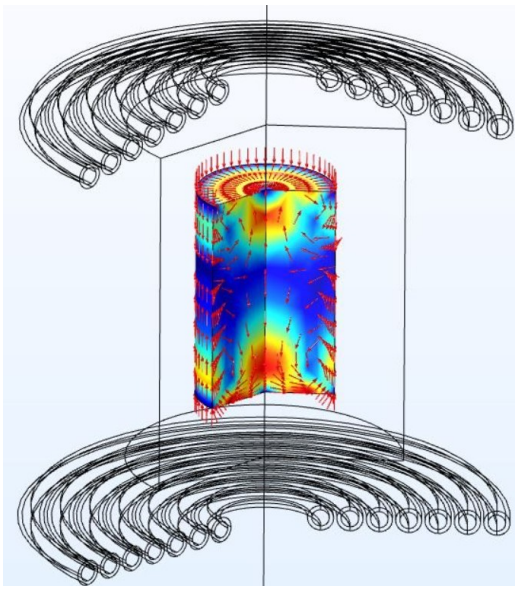

Figure 24: Comsol modulation of the movement in the γP field.

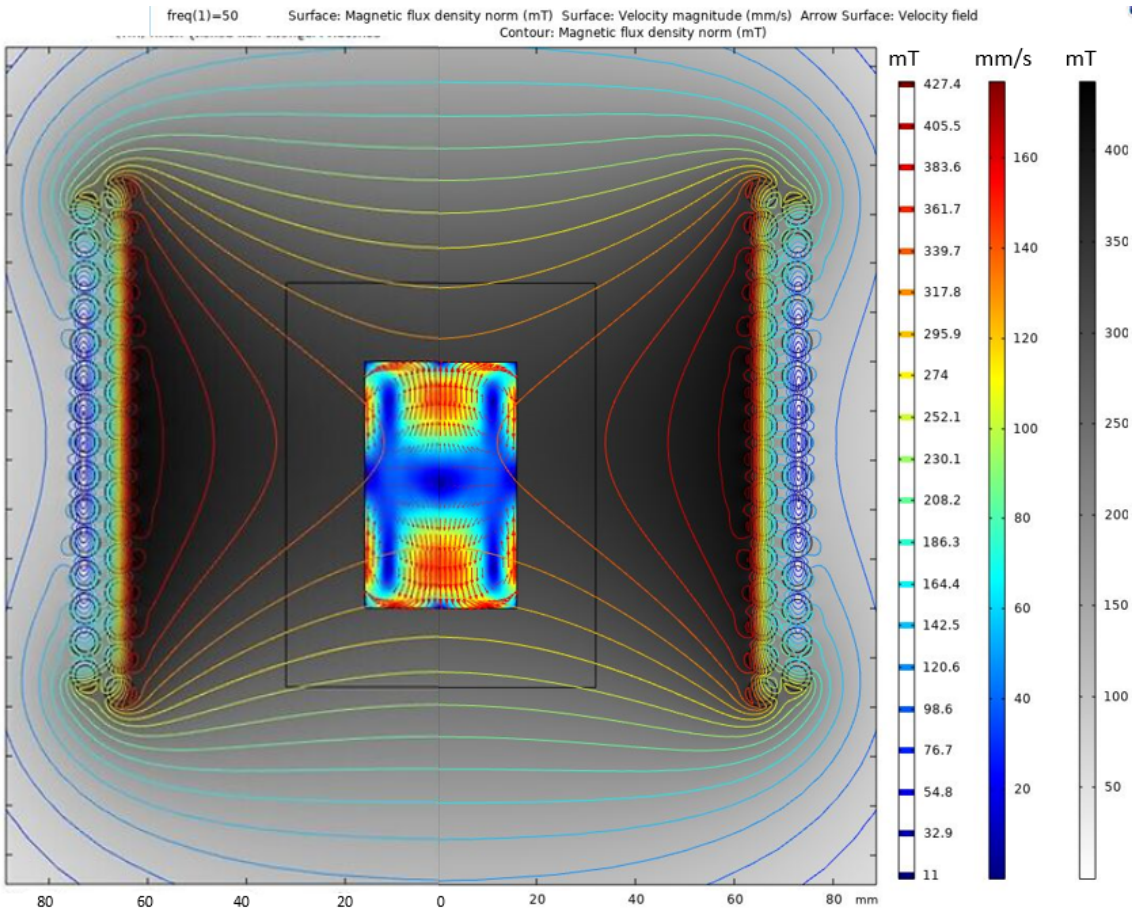

Figure 25: Comsol modulation of the R field.

4.3 Visual Inspection

One sample from the EM cast and one sample from the regular cast are shown in Figure 26. This picture shows a clear difference in both the surface texture and colour. The EM cast is darker and the surface is rougher compared to the regular cast sample.

Figure 26: Untreated EM cast and regular cast samples seen from the top and the side. The EM cast sample is darker in colour.

After having cast the samples, clear trends were identified based on appearance. The regular casting samples exhibited clear dimpling at the top of the samples, while some of the EMC samples had a narrowing at the sides. A likely factor causing this is the stirring in the liquid aluminium created by the magnetic field. This stirring causes the aluminium to flow towards the centre of the mould before circulating out along the top and bottom, as shown in Figure 24.

The regularly cast samples had a smooth surface with a metallic gleam and a dimple caused by molten metal at the top of the mould moving down to fill the reduction in volume caused by solidification shrinkage. The EMC samples had a rough, darker surface with no gleam. The EMC samples showed no sign of dimpling and had a very uneven surface at the top of the sample instead. This is where the metal was not in contact with the mould and the roughness is likely due to the movement of the molten aluminium caused by the magnetic field. As the magnetic field was maintained until complete solidification of the sample, the aluminium most likely solidified during movement. This would cause the metal to not move down and fill the lost volume from solidification shrinkage. This movement may also have compromised the BN coating inside the graphite mould, allowing more carbon from the graphite mold into the cast and affecting the sample colour.

After cutting, polishing, and anodising the samples, substantial defects were visible on the surface of the D and EMC samples. These surfaces are shown in Figure 27. The most common defect is pores, but some samples also have larger scratches on the surface. The most notable of these samples are Al-3-D, Al-αP, Al-R, AlSi7-2-D and AlSi7-R as they have a larger size and or number of visible defects.

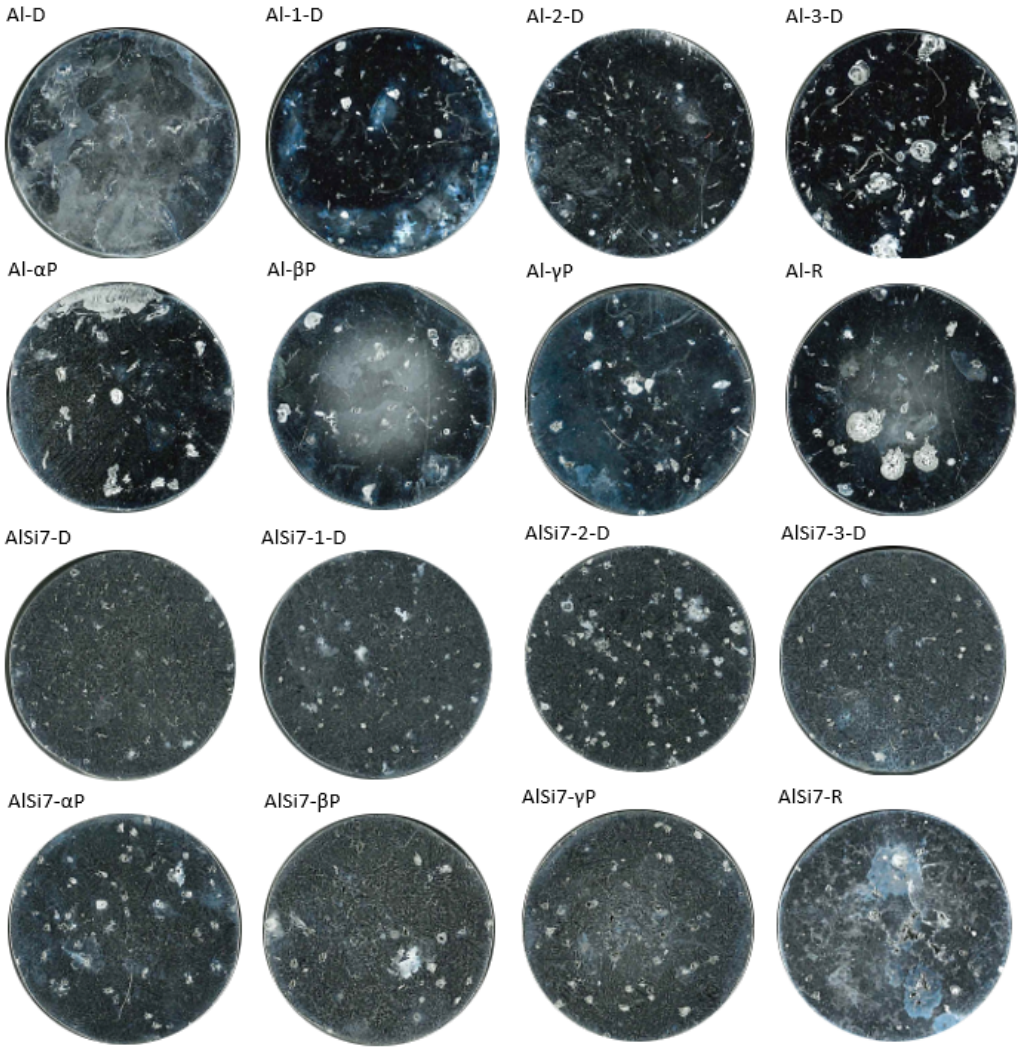

Figure 27: Photoscan of D and EMC samples showing defects on the polished surface.

The likely cause of the pores is dissolved hydrogen which forms H_2 gas during solidification. The gas bubbles nucleate at the grain boundaries or impurities during solidification and are usually found at the grain boundaries. A closeup of gas and shrinkage pores from AlSi7-1-D is given in Figure 28.

The D and EMC samples have a relatively long solidification time that enables larger hydrogen bubbles to form. These bubbles may then have become trapped by surrounding grains, resulting in large pores inside the samples. The EM casts have the lowest solidification rate of all samples, because the added energy from the electromagnetic fields can heat the molten Al inside the mold. The stirring caused from the fields could also be a contributing factor. This stirring action could cause hydrogen bubbles that form in the melt to be moved around while colliding and combining with other bubbles. While the bubbles are being stirred in this way, they may not be able to escape the melt and will be trapped once solidification happens. This would explain why the holes in the EMC samples are generally larger in size, compared to the D samples.

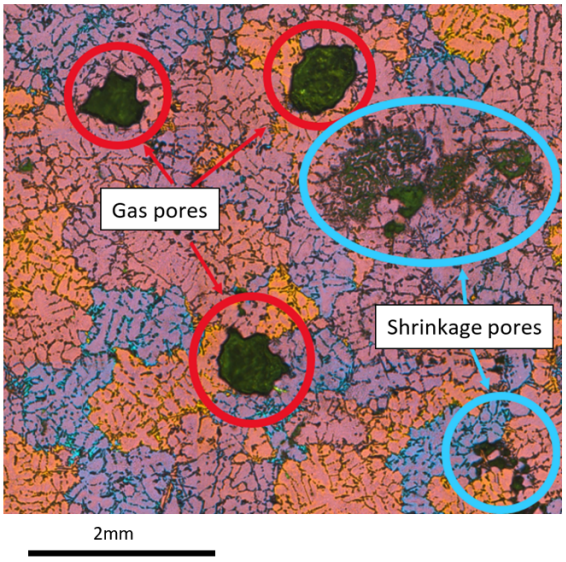

Figure 28: Gas and shrinkage pores found in AlSi7-1-D.

The A, B, and C samples had some pores as well. These were however very small in comparison to the D and EMC samples and were only visible under the microscope. The pores and holes created inconsistencies in the micro structure which resulted in less distinct grain boundaries. They also created areas where the grain analysis algorithm isolated a huge number of grains, which in reality was the space between pores. These results show the importance of degassing molten aluminium before casting samples and should be done even at lab scale. The reason inert gas degassing was not done for this research is due to not having the equipment needed.

4.4 Microscopy

Images acquired from polarised light microscopy makes it possible to distinguish between different grains and see the grain distribution within each sample, as well as pores or other defects. This process can be somewhat imprecise, but is a low cost and time saving alternative to an EBSD analysis. The different colours in the microscope pictures indicates different grain orientations. Areas with the same colour can therefore still contain more than one grain. If a grain has a changes orientation while it grows, the colour will therefore also change making it possible for one singular grain to have more than one colour. Grains with spills or marks affect polarised light differently than anodised aluminium.

4.4.1 Effect of Solidification Rate for Aluminium

Due to the differences in the moulds used for casting, the rate of solidification differs between the various sample types. The solidification rate of the samples decreases alphabetically from A to D. This difference is caused by the rate at which heat can be transferred away from the aluminium, which again is dependent on the thermal conductivity, specific heat and mass of the mould. The solidification rate for mould A and B is likely to be similar as they are both made of iron, thereby having the same thermal conductivity. Different solidification rates are therefore a result of differing volume of liquid metal and mass of the mould. Because mould A has a larger mass, it can receive more thermal energy from the sample without increasing its own temperature as much as mould B. Thereby maintaining a higher gradient giving a more rapid cooling. Mould B has a different shape than the three other moulds. It is a disk instead of a cylinder, and is also the only sample where the metal has contact with a lid at the top of the mould. This will likely cause a difference in solidification mechanisms.

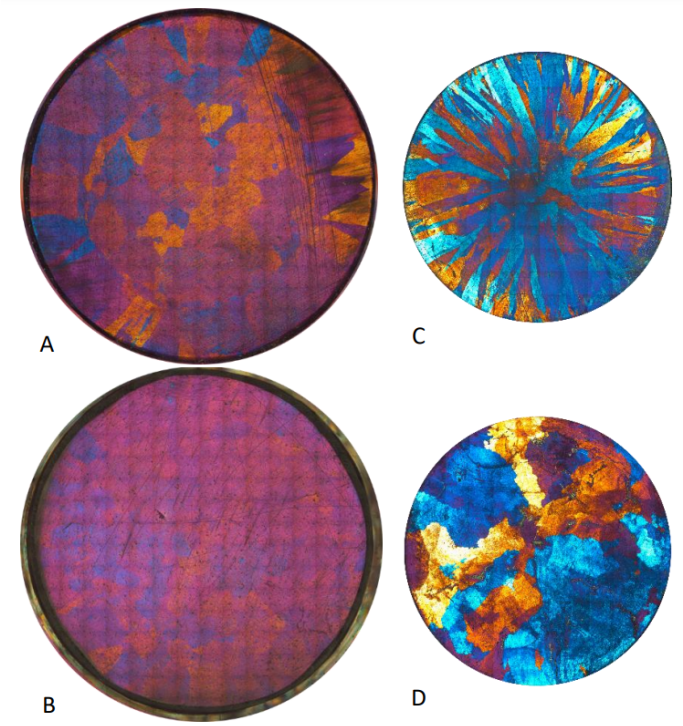

Figure 29 contains the polarised light microscope images of whole surfaces of the A, B, C, and D samples of Al without grain refiner. Al-C and Al-D show clear indications that solidification instigates at the interface between the mould and the liquid Al. The samples begin solidification at the edges and the grains grow inwards towards the centre, creating long thin grains. Al-D had the lowest solidification rate, and the grains therefore had more time to grow in size, resulting in large grains which reached from the edge to the middle of the sample.

Figure 29: Pure Al samples from the four different moulds.

Al-A also has indications of grain growth starting from the edges. However, approximately 5 mm from the edge of the mould a more uniform grain pattern is observed. This pattern could be caused by the moulds shape, where the bottom is thicker than the walls encouraging faster solidification from the bottom since this area can conduct more heat. Al-B has a lower solidification rate than Al-A and more grain growth converging towards the centre are therefore expected. However, no such convergence is seen in the Al-B sample. This is likely caused by the difference in mould shape. While mould A has the same relative shape as C and D, mould B is considerably different. Mould B creates a disk-shaped sample as opposed to a cylindrical shaped one. This entails a larger interface between sample and mould at the top and the bottom of the mould, rather than at the sides as it is for mould A, C, and D. Therefore, the growth mechanisms for mould B differs from the others. Despite the difference in solidification rate the structure within the grains are relatively similar. Closeups of the pure Al samples are shown in Figure 30.

The grains appear long and thin, reaching from the edge toward the center of the sample. A similar effect is to be observed in the Al-D sample. This effect is a result of Al only solidifying into one phase and having low enough solidification rate to slowly solidify inwards, and at the same time produce long and relative big grains. Most variations seem to stem from either surface porosity or poor sample preparation resulting in scratches.

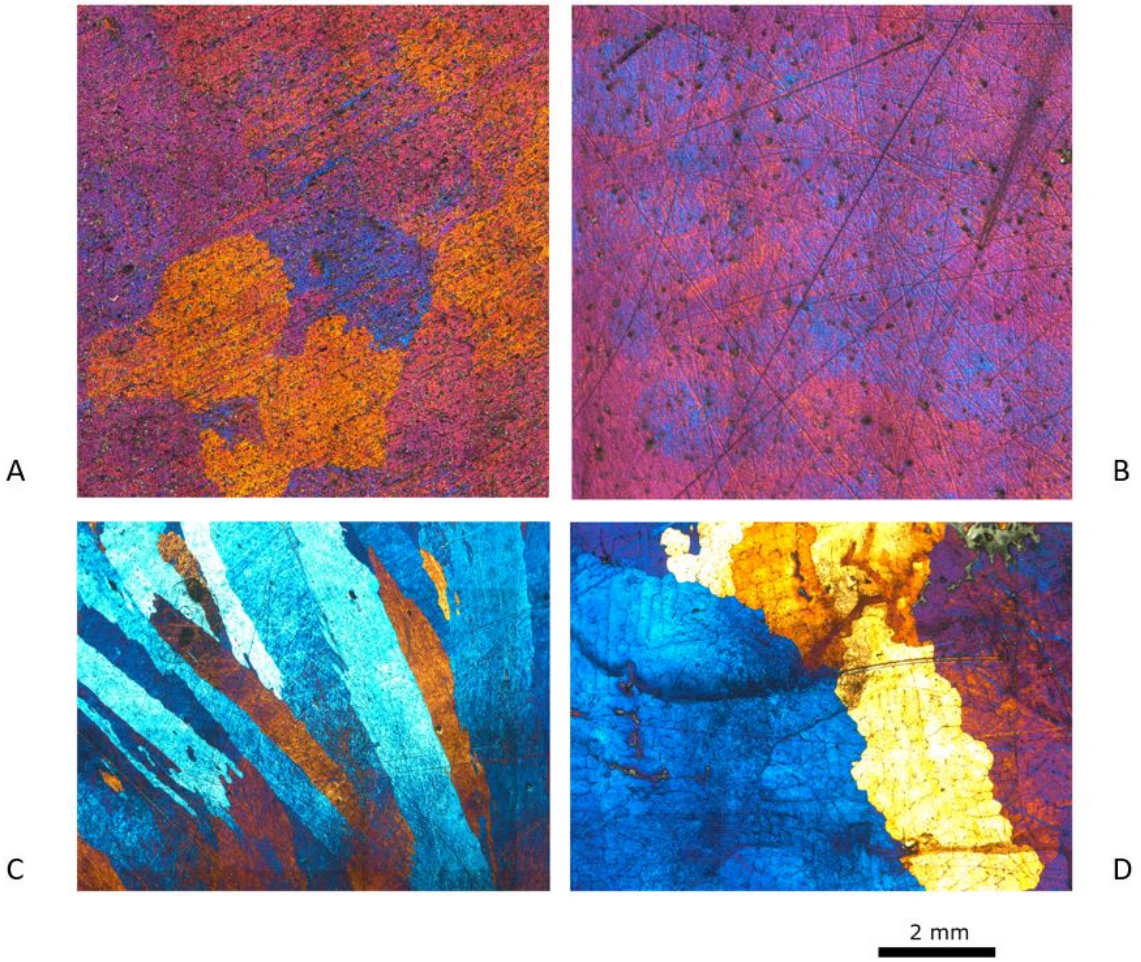

Figure 30: Closeups of the pure Al samples.

A higher magnification of Al-A, Al-B, Al-C, and Al-D is shown in Figure 30. Al-A, Al-B and Al-C show no sign of dendritic structure. Al-D does however show a more textured grain structure. This less uniform grain structure is the result of dendritic growth. Dendrites had more time to grow as sample D had a lower solidification rate than the other samples. This allowed for more prominent dendritic structures to form. Samples from mould C and D mostly solidified from the side wall due to the shape of the mould whereas mould A and B have high thermal conductivity through the bottom as well. This, as well as the higher solidification rate, resulted in grains that are more rounded compared to Al-C and Al-D.

The solidification mechanisms promoted by a cylindrical mould may affect the results gathered based on where on the sample an analysis is conducted. Therefore, Al-C and Al-D samples were also cut into rectangular cross sections, Al-CX is such a sample and is shown in Figure 31. Al-CX clearly indicates how solidification in the sample instigates at the sides and bottom, where the cast interfaced with the mould. Al does not have multiple phases, where one phase can solidify first and act as a seed. Therefore, nearly all grains start to grow from the edges of the sample. This causes lines from the sides and bottom stretching towards the center of the sample. In addition, there clearly are core grains stretching vertically through the sample from the top of the sample to the grain growth instigated from the bottom of the sample. This image shows why it is important to cut the circular cross sections around two thirds up from the bottom. The height at which the sample is investigated will affect how much grain growth from the bottom is observed.

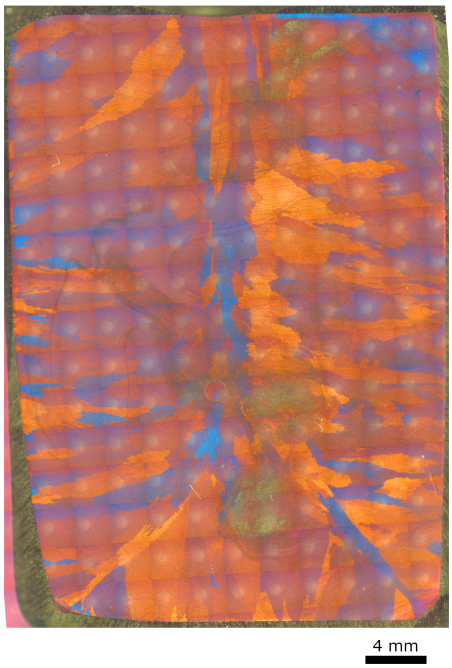

Figure 31: Rectangular cross section of the pure Al C sample (Al-CX).

4.4.2 Effect of Solidification Rate for AlSi7

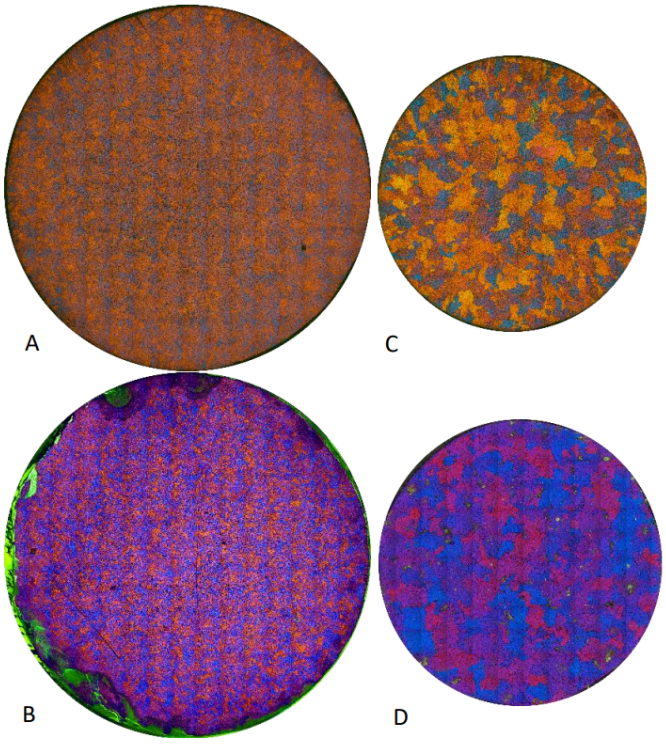

Figure 32: Pure AlSi7 samples from the four different moulds.

Figure 32 shows AlSi7 alloy with no added grain refinements solidified at four different rates. Here we do not see the same growth characteristics in the C and D samples as in the Al. Though the grain sizes are slightly smaller at the edges, there is no convergence towards the centre of the sample. This is due to the different solidification process caused by the addition of silicon. Figure 6 illustrates how at 7wt% silicon, AlSi7 will create a partly solidified zone during solidification. These partly solidified areas will be spread throughout the sample and act as seeds for solidification. Thereby, causing a more uniform grain growth throughout the sample and not just from the edges and inwards.

The full sample images are too large to achieve an accurate understanding of the micro structure within the separate grains. Figure 33 shows a higher magnification image of AlSi7-A, AlSi7-B,

AlSi7-C and AlSi7-D.

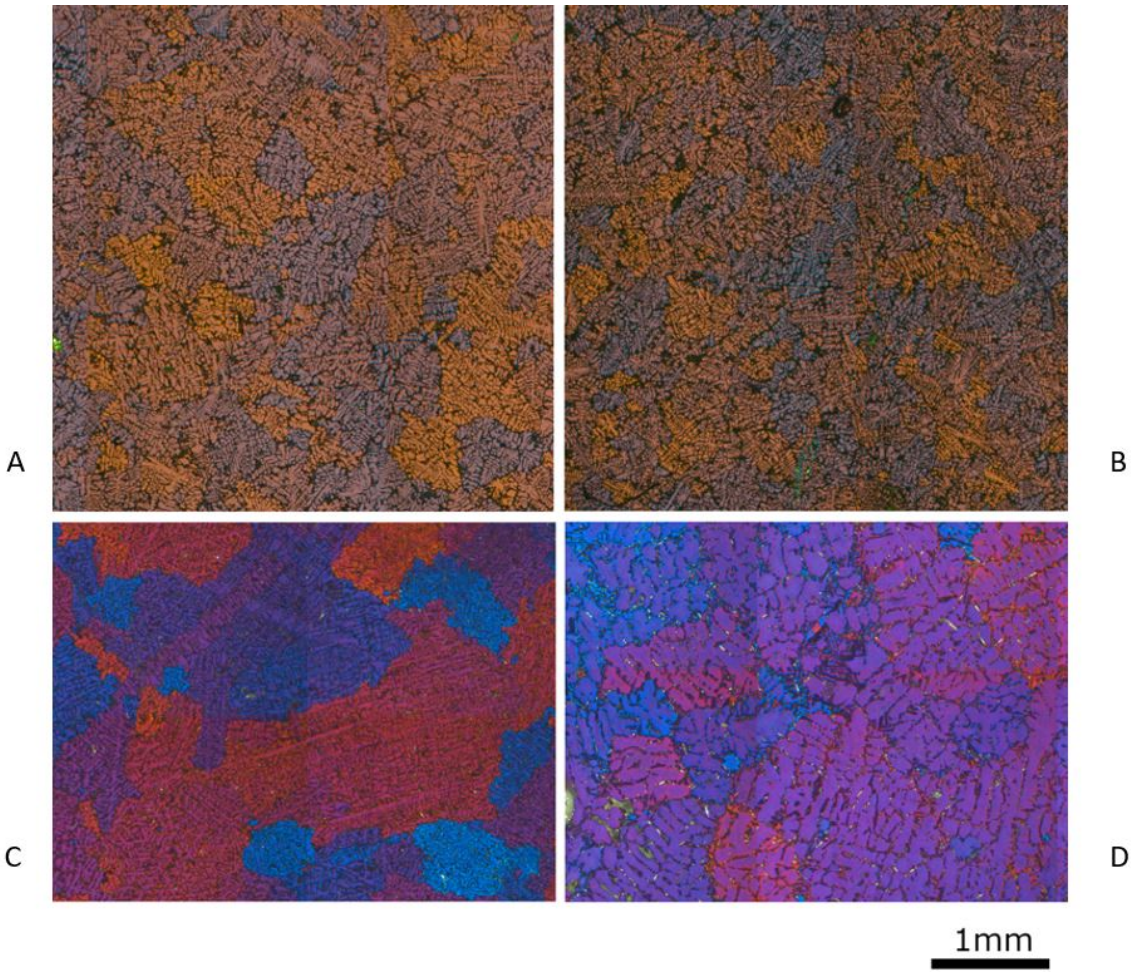

Figure 33: Higher magnification images of the pure AlSi7 samples.

From the closeup of the pure AlSi7 alloy in Figure 33 it can be observed that the grains are more similar and uniformly spread than those of Al shown in Figure 30. The grains also appear smaller for all AlSi7 samples than those of Al.

All AlSi7 samples have a clear dendritic growth as opposed to Al. This is not nearly as evident in the Al samples because of the large solidification range of the alloy, α-Al phase will start to nucleate and solidify early in the solidification process. This mix of molten and solid is called a mushy zone, and leads to a longer solidification time that allows dendrites to grow bigger. The shrinkage of molten and solid metal when it cools down causes voids when the alloy solidifies. These voids make the dendritic growth structure more clear.

4.4.3 Inspection of Grain Refiner

For comparing the effect chemical grain refiners have on grain size, they were each inspected in SEM. The distribution of TiB_2 particles did not vary substantially across the surface. One 200X magnified imagine from the centre of each sample surface is shown in Figure 34. The images were captured using an SE2 detector that has a compositional contrast where heavier elements are lighter. Using EDS point scans the lighter particles were determined to consist of titanium, and the dark background aluminium. Although no boron was detected, it is assumed that the lighter particles are TiB_2 clusters. This is because EDS cannot detect lighter elements like boron.

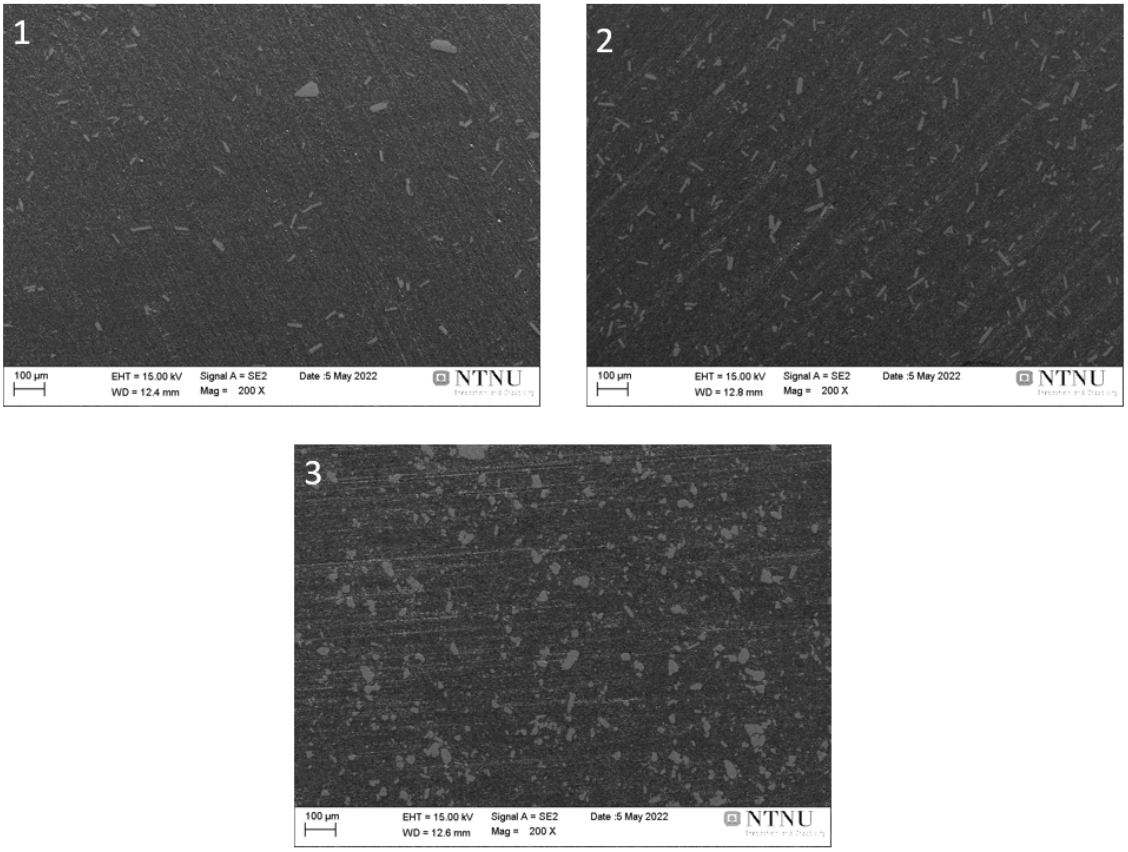

Figure 34: Samples of pure grain refiners at 200X magnification: 1 - KBM $AlTi_3B_1$, 2 - GR $AlTi_3B_1$, 3 - Aleastur $AlTi_5B_1$

The TiB_2 particles should ideally be thin and pointy to promote growth of fine grains in Al. The $AlTi_5B_1$ grain refiner contains more particles, but they are also more rounded compared to the $AlTi_3B_1$ grain refiners. The KBM $AlTi_3B_1$ grain refiner also has noticeably less particles compared to the GR $AlTi_3B_1$ grain refiner.

4.4.4 Effect of Grain Refiner

The samples containing grain refiner generally have smaller grains. All A, B, C, and D samples with commercial pure Al are shown in Figure 35. The columns represent the different moulds, while the rows represent different grain refiners. The blank row is Al without grain refiner, row "1" is with KBM $AlTi_3B_1$, row "2" is with GR $AlTi_3B_1$ and row "3" is with Aleastur $AlTi_5B_1$.

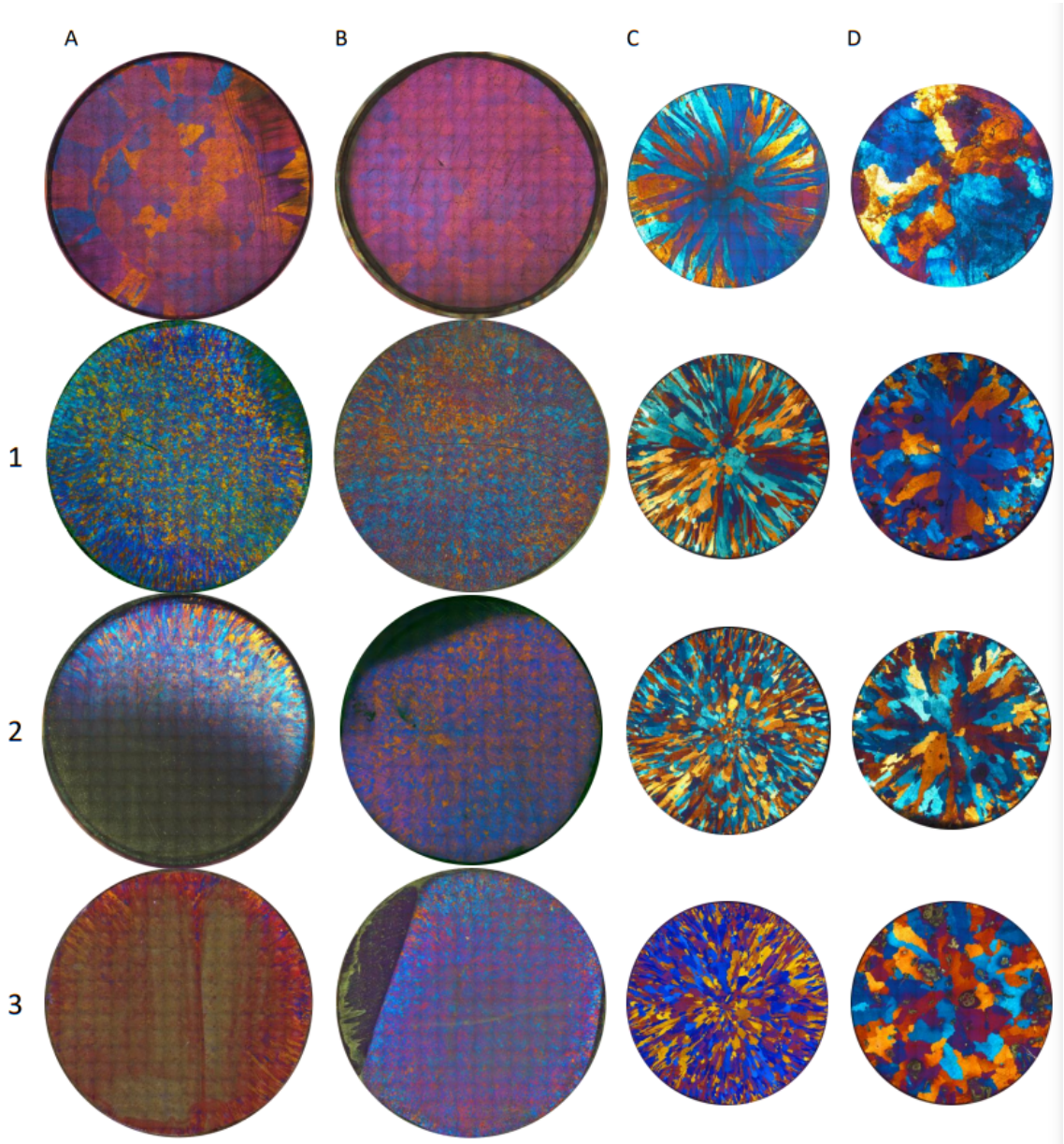

Figure 35: Al A, B, C and D samples with and without grain refiner.

The Al samples with grain refiner follow the same trend as shown in the Al and AlSi7 samples, namely having coarser grain shapes with a better insulated mould. Though the images of some samples, such as Al-2-A and Al-3-A are somewhat unclear, the trend seems to be uniform throughout the samples. The unclear areas in some of the pictures are likely due to the samples being compromised during polishing and anodising. The C and D samples with grain refiners also seem to solidify from the edges and converge towards the centre of the sample, while B samples do not. This is consistent with the theory that the disk-shaped B mould will solidify mostly from the top and the bottom and not from the edges. The A samples do show some grain characteristics that are similar to that of C and D. At the edge of each of all Al-A samples there is a small region where grains seem to grow from the edges converging towards the centre. The addition of grain refiner does not seem to affect the convergence of grains towards the center of the samples.

In a similar study (Hassanabadi 2018 [3]) the effect of Al-3Ti-1B and Al-5Ti-1B grain refiner on commercial pure Al 99.7% cast in an iron mould was studied. The result of their study is therefore most relevant to compare to the Al-A samples with grain refiner additions. In the study the samples were cast at 0, 30, 60, and 90 minutes from addition of the grain refiner. The reduction

in grain size are not as substantial as observed in Figure 29. The particles in the grain refiner agglomerates when in the liquid Al, reducing its efficiency. Therefore, the difference in grain size is likely a cause of the time difference to this study.

All A, B, C, and D samples of AlSi7 are shown in Figure 36. The columns represent the different moulds, while the rows represent different grain refiners. The blank row is AlSi7 without grain refiner, row "1" is with KBM $AlTi_3B_1$, row "2" is with GR $AlTi_3B_1$ and row "3" is with Aleastur $AlTi_5B_1$.

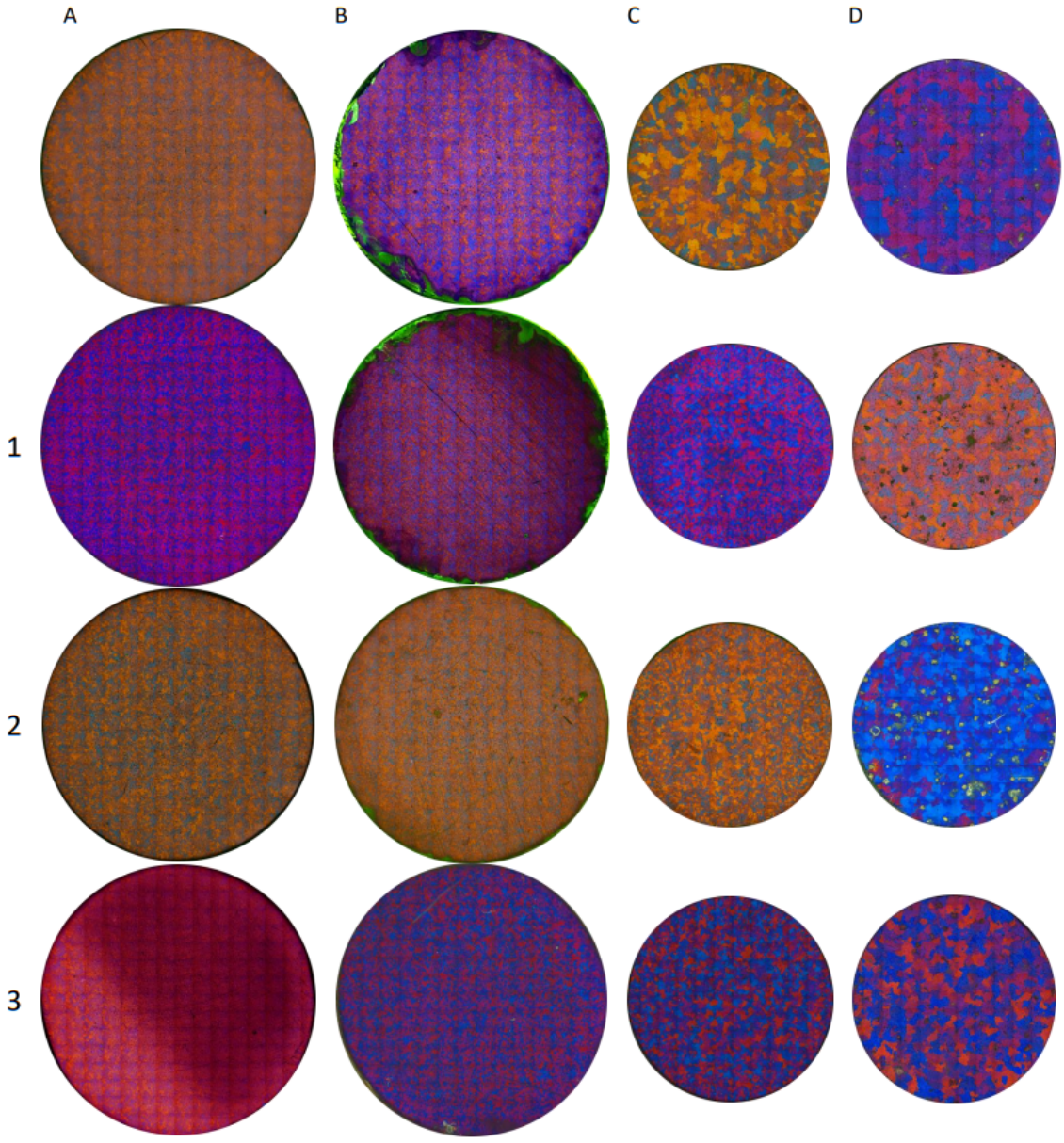

Figure 36: AlSi7 A, B, C and D samples with and without grain refiner.

With a decreasing solidification rate, an increasing grain size is seen throughout all grain refinement additions to AlSi7. The difference in grain size when adding grain refiner to AlSi7 is not as substantial compared to Al. Especially for the AlSi7 A and B samples, the difference in grain size with and without added grain refiner is not determinable by analysis. However a difference in grain size can be observed for the AlSi7 C and D samples. In general, the grains are more uniformly spread throughout the sample and do not follow the same inward growing pattern that was observed for Al. The colour palette for the AlSi7 samples are less diverse, this can imply that

the grains are more similarly oriented, but this theory would need further exploration in order to be confirmed.

4.4.5 Effect of EM Fields

The surfaces of circular and rectangular cross sections of the samples from the pancake coil and the round coil casts are shown in Figure 37 for Al and Figure 40 for AlSi7. In the figures the field strength increases from left to right. The field strength measurements for each sample type is shown in Appendix B

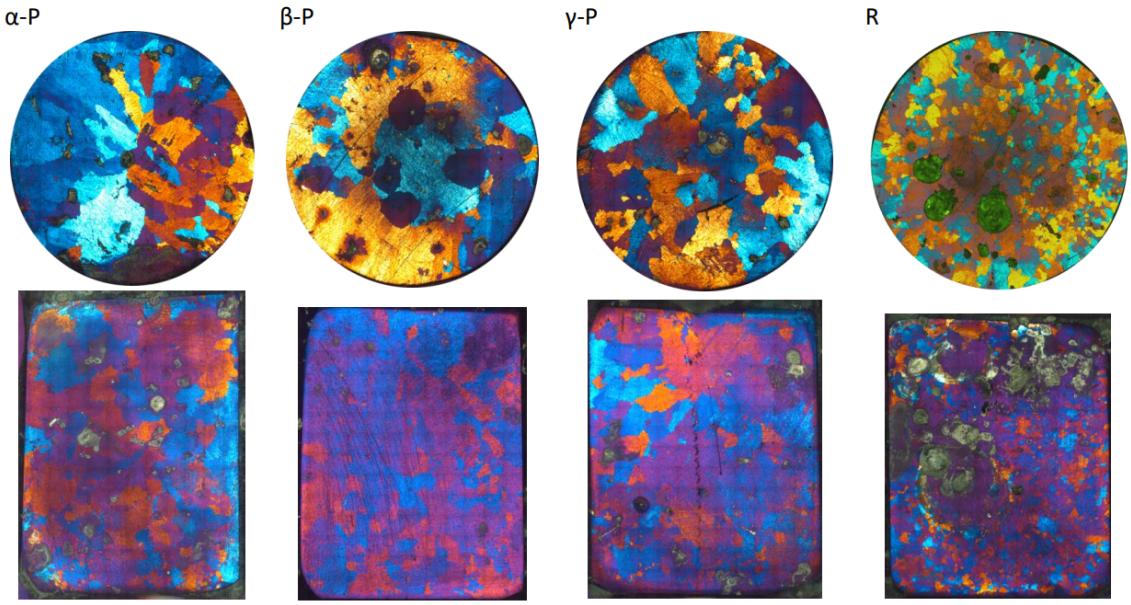

Figure 37: Al pancake (P) and round (R) coil field samples.

The rectangular cross section of the Al sample from the D mould is shown in Figure 38. From this figure it can be seen that the grains are bigger than for the EMC samples. The effect of electromagnetic stirring during solidification is clearly shown, as the EMC sample show no sign of dimpling, whereas a large dimple can be seen in the Al-DX sample, caused by the directional solidification from the sides of the moulds towards the middle of the sample. In addition, the grains in the EMC samples does not show directional grain growth like Al-DX does.
A comparison between the circular cross sections of Al-D and the EMC samples are shown in Figure 39. Al-D is compared with these samples, as they all have the same composition and the most similar solidification rate.

Figure 38: Pure Al rectangular cross section D sample (Al-DX).

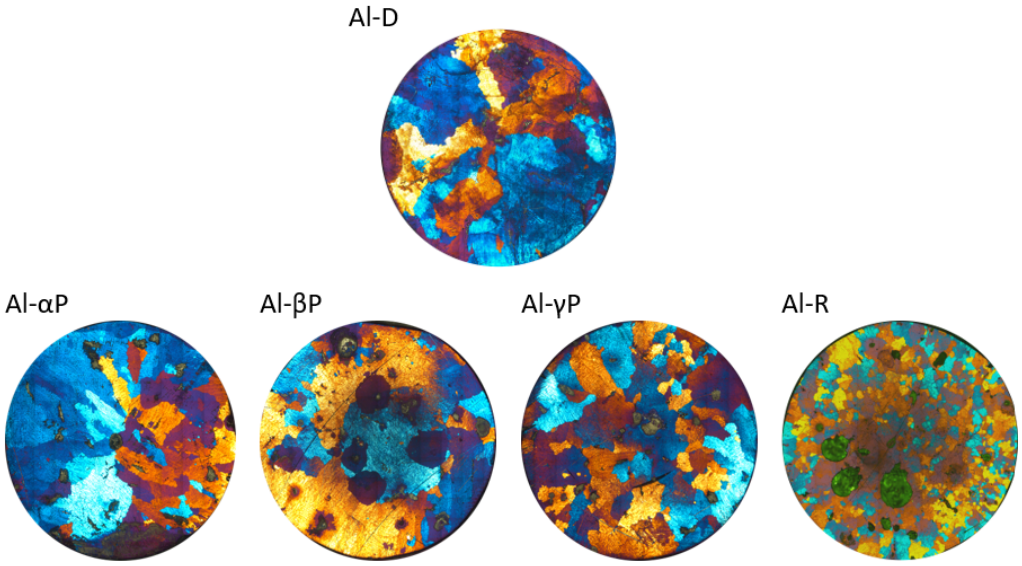

Figure 39: Al D and EMC samples.

Though the samples have clear imperfections, it is evident that increasing the EM field strength reduces grain size a considerable amount. The parts of Al-R that are easily visible, show a clear reduction in grain size in comparison to Al-D as a result of the EM field. This is supported by the fact that Al-γP has a noticeably smaller grain size than the two other P samples. While Al-αP may seem to have some smaller grains than Al-βP, this could be a result of two aspects. Firstly, the samples may simply have been cut at a slightly different heights. As seen in the rectangular cross sections in Figure 37 the grain size change a considerable amount throughout the height of the sample. Secondly, the difference in effect of the EM fields could be so low that it becomes negligible. However, without more samples to compare with, a more accurate trend cannot be determined.

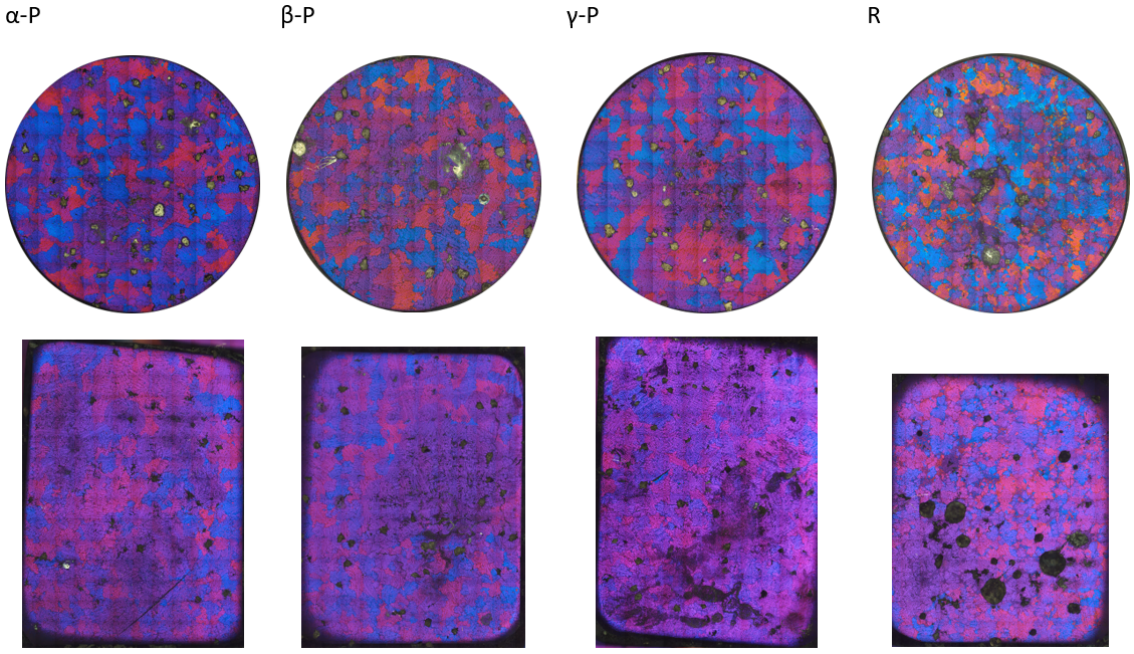

Figure 40: AlSi7 pancake (P) and round (R) coil field samples.

The grain size differences between the six P samples, shown in Figure 40, are to small to determine if there is any changes in grain size with different field strengths generated by the pancake coil.

AlSi7-R and AlSi7-RX does however show a substantial reduction in grain size when compared to the P samples. This indicates that EM fields has an effect on grain size in AlSi7, but requires a higher field strength compared to Al.

A comparison between AlSi7-D, and the EMC samples are shown in Figure 41. AlSi7-D is compared with these samples, as they all have the same composition and the most similar solidification rate.

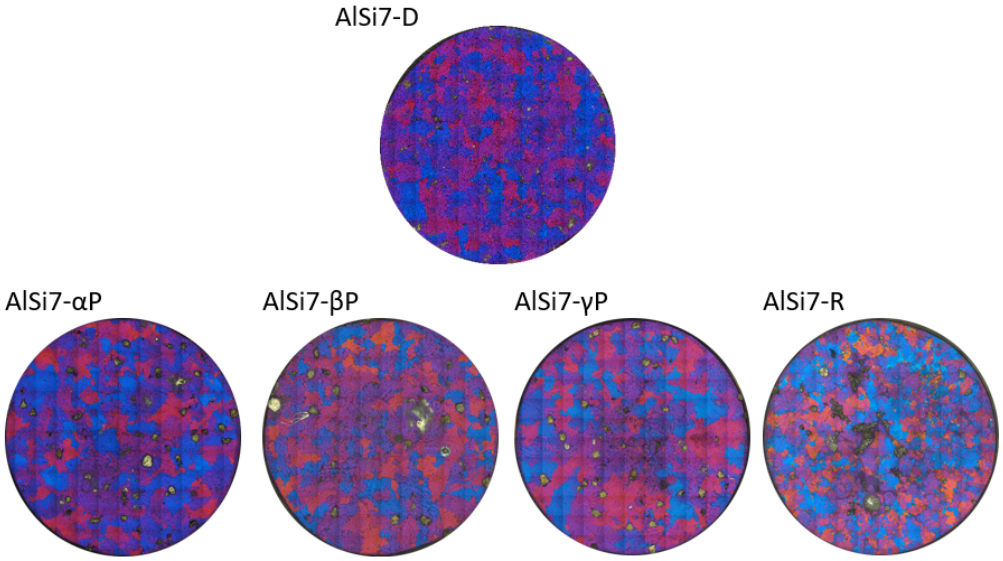

Figure 41: AlSi7 D and field samples.

This figure shows that AlSi7 does not seem to have any considerable grain refinement effect from the P EM fields at all when compared to AlSi7-D. This is likely due to the mushy zone in AlSi7 lowering the efficiency of the EM stirring by quickly dissipating the stirring movement as the solid - liquid mix is a lot more viscous compared to molten Al. However AlSi7-R has considerably smaller grains compared to AlSi7-D, supporting the initial assumption that the higher field strength would reduce grain size considerably compared to weaker fields. The same effect has been observed in an experiment conducted by V. Metan [1] where it is stated that "an increase of the field intensity provokes a distinct grain refinement, a homogeneous distribution of fine grains..." [1].

AlSi7-R also have areas with a needle like structure. One of these areas are shown in Figure 42.

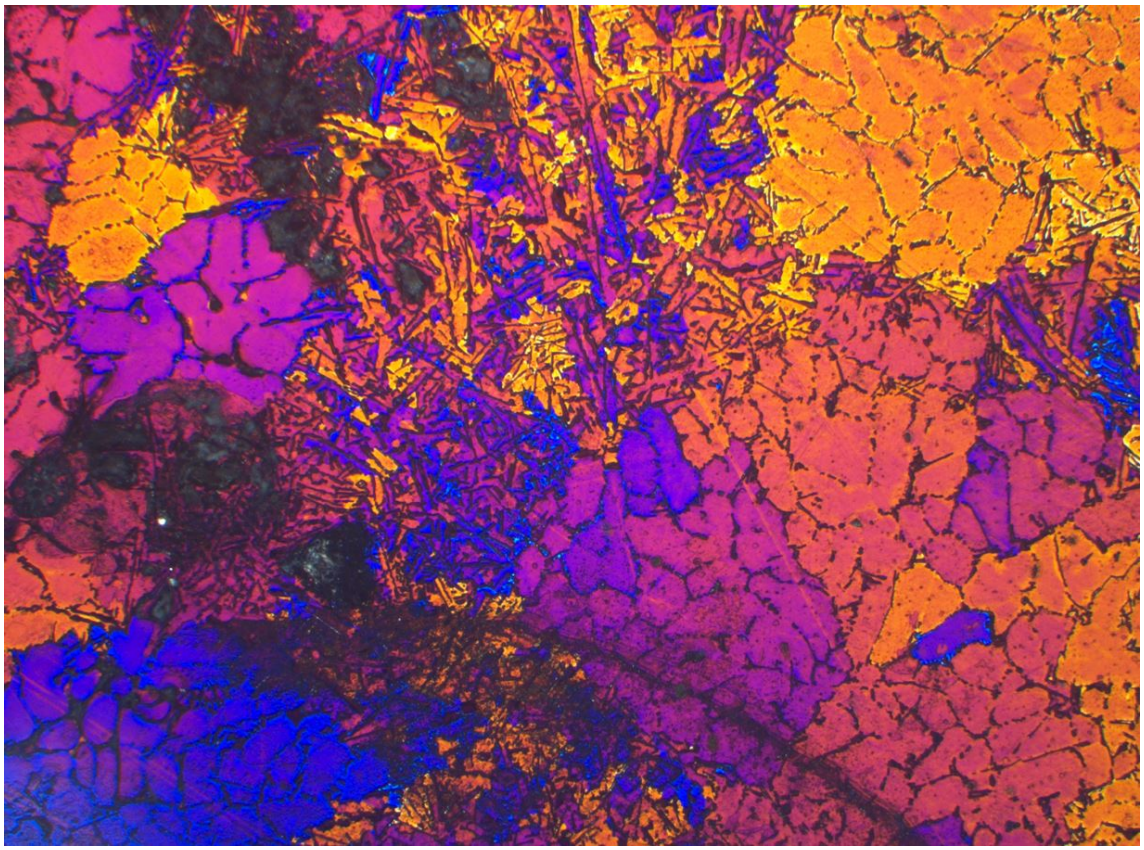

Figure 42: Eutectic zones created by strong EM stirring in AlSi7-R.

A clear difference in the microstructure of the material can be observed in AlSi7-R. There are numerous smaller grains that have a more needle like shape spread across the entire sample. This structure is likely the result of eutectic zones. During solidification in AlSi7, $\alpha - Al$ starts to solidify first. This causes the Si concentration to increase in the remaining melt until it reaches an eutectic concentration and solidifies. This eutectic concentration usually solidifies at grain boundaries. Because of the strong EM stirring in AlSi7-R, the molten eutectic Al - Si will be separated from the solidified $\alpha - Al$ and form zones. This process continues until most of the sample has solidified, and the molten eutectic zones solidify in the needle like structure seen in Figure 42. This development was only present in the AlSi7-R and AlSi7-RX sample and was observed throughout the samples. However in the image with higher magnification of AlSi7-D shown in Figure 33 does show some amount of needles in the grain boundaries. This supports the theory that these needles are eutectic Al - Si that has solidified. This is because as the AlSi7-D has larg grains compared to the other AlSi7 samples, the concentration of Si reaches eutectic in the grain boundaries of some areas. This local increase in alloying elements was also observed, and then measured in a study (Ruvalcaba, D et al 2007 [3]) looking at dendrite fragmentation.

4.5 Grain Size Analysis

The grain size analysis algorithm yielded an average grain size for the C, D and EMC samples that was determined to be accurate enough for a meaningful comparison between these samples. These values were in turn plotted based on sample type. The plots for the C samples for both Al and AlSi7 are shown in Figure 43, where the gray graph represent AlSi7 and the yellow Al. This data is shown in Appendix D.

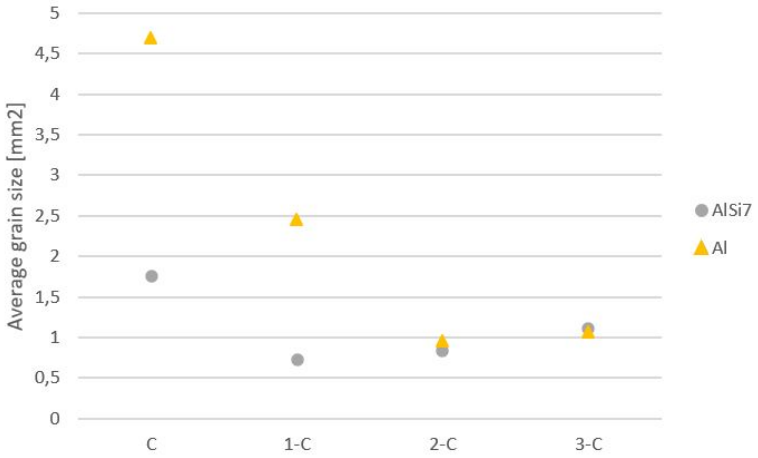

Figure 43: Average grain size for C samples of Al (left) and AlSi7 (right).

For both Al and AlSi7, the C sample without grain refiner has substantially larger average grain size than samples containing grain refiner. This is expected as the grain refiner initiates solidification evenly throughout the sample. The difference is of more prominent scale between the Al than the AlSi7 samples, the same effect can be seen in Figure 35 and 36. The less notable difference in grain size for AlSi7 samples with and without grain refiner is caused by the mushy zone that occurs during the solidification of AlSi7, leading to more uniform grain distribution throughout the sample. Both grain refiner 2 and 3 have approximately the same average grain size independently of the alloy.

The Al-D samples were plotted together with the EMC Al samples in order to properly observe the difference in effect. These values are seen in Figure 44. This data is shown in Appendix D.

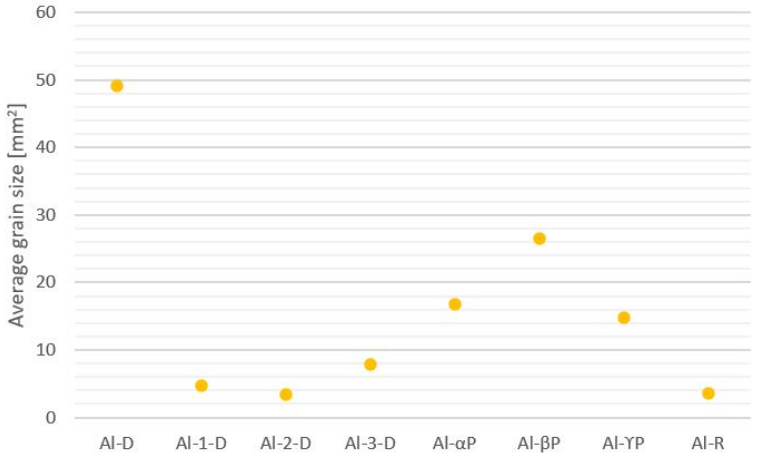

Figure 44: Average grain size for D samples (left) and EMC samples (right) of Al.

As shown in Figure 44, the Al sample without grain refiner or influence of a magnetic field has the highest average grain size. This is as previously observed in the comparison of the micro structures in Figure 39 for D and EMC samples and Figure 35 for the grain refiners. From the graph it is clear that the R sample has lower average grain size than the other three EMC samples, being within the same grain size range as samples containing grain refiner.

In order to compare effects of grain refiners and EMC, the grain size AlSi7-D samples were plotted together with the EMC AlSi7 samples. This plot is shown in Figure 45. This data is shown in Appendix D.

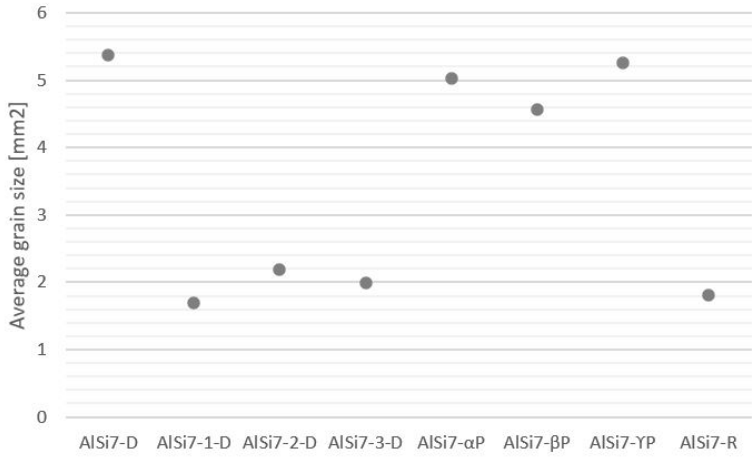

Figure 45: Average grain size for D samples (left) and EMC samples (right) of AlSi7.

As seen in Figure 45 the EM P fields have not affected the average grain size of AlSi7 considerably compared to the effect of grain refiner or the EM R field. The effect of grain refiner and the EM R field appears to have had similar effects on the average grain size with around 2 mm^2 for all these four samples. This can be observed from Figure 44 as well, where the R sample has close to the same average grain size as the grain refiner samples. EM fields are therefore an option for chemical grain refiners in terms of grain refinement.

The increase in grain size from the C to D samples with grain refiner is likely a result of the particles in the grain refiner agglomerating more as the temperature is higher for a longer time span for the D samples. The lower solidification rate gives the grains more time to grow and the solidification rate itself can therefore also be a reason, as this effect is seen for the samples without grain refiner as well.

4.6 Electrical Conductivity

The conductivity measurements of all samples are given in Figure 46. Where yellow represents samples of Al and gray AlSi7. The samples of the two alloys are sorted based on increasing conductivity from left to right. The samples labelled with an X are samples with rectangular cross sections. These rectangular cross section samples are unsuitable for comparing with the circular samples, all cut around the same height. This is because the grain structure and the volume of pores is considerably different throughout the height of the samples as shown in Figure 31, 37, 38 and 40. The conductivity data used to plot the graphs are given in Appendix E.

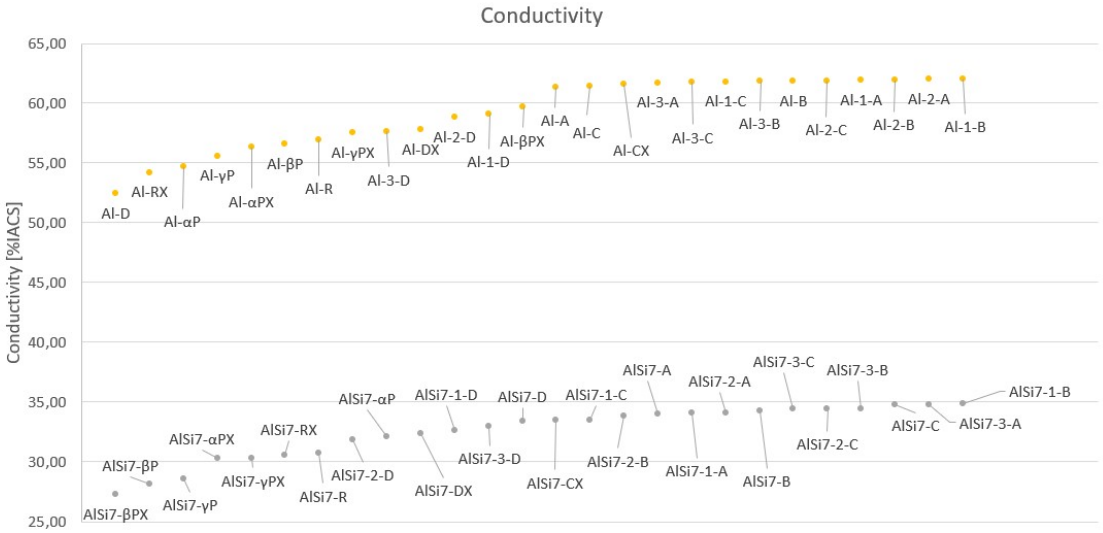

Figure 46: Conductivity measurements for all Al and AlSi7 samples sorted by increasing conductivity.

Figure 46 shows that all samples of Al have a higher conductivity than those of AlSi7, with a considerable margin of at least 15 %IACS. On average the Al samples have almost twice the electrical conductivity of the AlSi7 samples. The reason for this difference is the addition of silicon as an alloying element. The silicon metal binds more strongly to electrons, increasing the alloy's electrical resistance compared to aluminium.

Figure 47 shows a plot of the average conductivity in each sample type for both alloys. The plots show that on average the highest electrical conductivity measurements are from the Al A, B, and C samples and that they fit well within the theoretical range of 59.5 - 63.9 %IACS. The other Al sample types fall short of the theoretical range by 2 - 4 %IACS. For AlSi7 the highest electrical conductivity measurements are also from the A, B, and C samples. These measurements are around 4 %IACS lower than the theoretical range of 38.3 - 40.1 %IACS. The other AlSi7 samples measured even lower at 5.5 - 9 %IACS below the theoretical range.

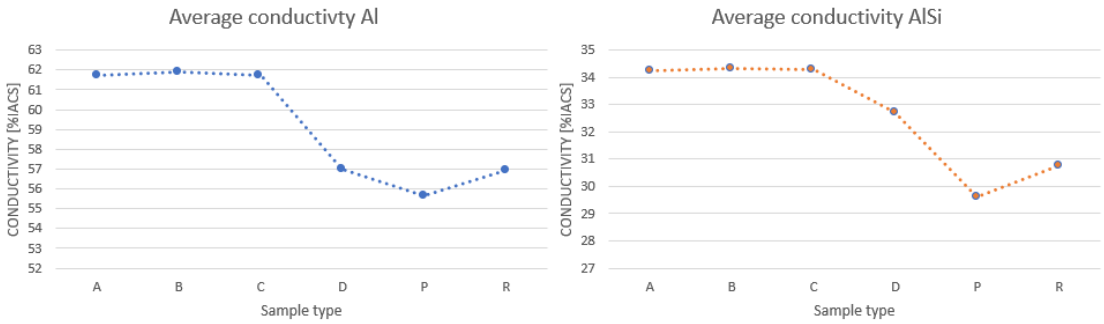

Figure 47: Average conductivity for each sample type of Al and AlSi7.

There are a lot of factors that could be the reason for no AlSi7 conductivity measurement to be within the theoretical range for conductivity. As seen in Figure 33, the AlSi7 alloy has very pronounced dendrites and small voids within each grain. This is likely to increase the resistivity of the samples as the current either needs to cross more grain boundaries or take a more convoluted path through the grains to avoid more boundaries. It is also possible that the height of the sample we analyzed was prone to a high concentration of intermetallics or that the calibration of the electrical conductivity meter was not correct. These are likely some of the main contributors for why the AlSi7 measurements were lower than the expected values.

The plot also shows that overall the EMC and D samples have the lowest conductivity. These samples also have a considerable number of pores as seen in Figure 27 compared to the other samples. These pores filled with insulating air caused the conductivity value to change a considerable amount depending on where the probe was placed on the sample. This made it problematic to get accurate measurements for the conductivity of the whole sample, but was somewhat mitigated by taking multiple measurements of each sample. However these pores are likely to be a main contributing factor for the substantially lower conductivity in these samples. If the Al was degassed before casting, it would be expected to see a considerable increase in conductivity, especially for the D and EMC samples.

For both Al and AlSi7, the differences in measured conductivity for A, B, and C samples are very small, especially for the ones with added grain refiner. More samples are required to determine if there is a statistically significant trend between these sample types.

Figure 48 show the measured conductivity value for every Al sample type and are plotted with increasing conductivity from left to right Figure

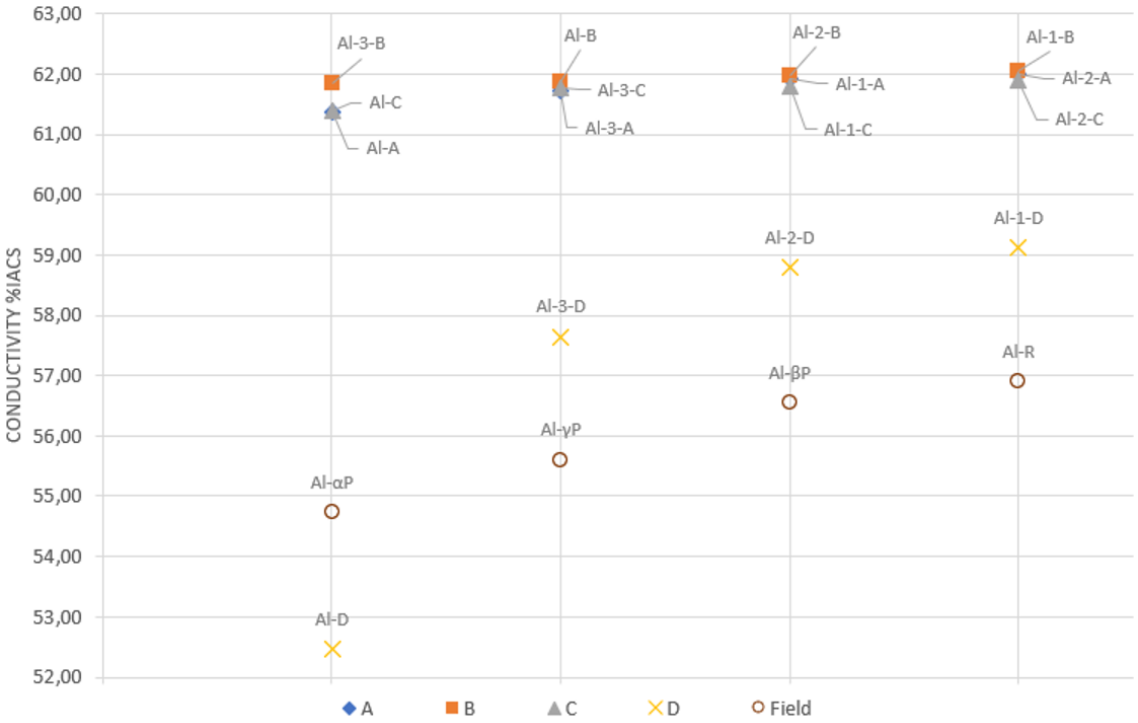

Figure 48: Conductivity measurements for Al sorted by increasing conductivity.

This plot shows that all of the samples with grain refiner have a higher conductivity than pure Al, except for Al-3-B which is slightly lower than Al-B. Note that the two best conducting samples for A, B, C, and D contains either grain refiner 1 or 2. Both of these are $AlTi_3B_1$ grain refiners, and has a higher conductivity compared to the rest of its type, especially for the D samples. This indicates that $AlTi_3B_1$ grain refiners have the highest combined positive effect on conductivity. The reason why Al with no grain refiner has a low measured conductivity is likely because of the larger grains in these samples. Adding grain refiners is similar to adding artificial contamination and particles which would usually lower the conductivity. The conductivity gained from the much smaller grain size does however seem to outweigh the loss caused by this contamination.

The highest performing sample for both Al and AlSi7 is the 1-B sample. These are RSD samples containing KBM $AlTi_3B_1$ grain refiner. The higher conductivity could be due to the solidification characteristics of the RSD samples affecting grain structure positively. In addition, the thin RSD samples may increase the odds of gas bubbles escaping before the sample solidifies, thereby reducing the volume of pores in the sample. The KBM grain refiner also contributes to the higher

conductivity by reducing the grain size in these samples.

Amongst the circular EMC samples the Al-R sample has the highest conductivity and Al-αP the lowest. They all have a higher conductivity compared to the Al-D sample. This is as expected from the visibly smaller grain size of the EMC samples. Al-βP is notable due having the largest grains of the Al EMC samples, but it still has a higher conductivity compared to Al-αP and Al-γP. This is likely caused by a larger volume of pores in Al-αP and Al-γP compared to Al-βP and further confirms the importance of degassing aluminium before casting.

The Al samples containing $AlTi_3B_1$ grain refiner from different producers have the highest conductivity for each sample type. This wt% of titanium therefore appears to have the best effect on conductivity for Al. The Al-3 samples, which have additions of $AlTi_5B_1$ grain refiner, have the lowest measured conductivity compared with all other samples with grain refiner, however they are still higher than the samples with no grain refiner added, except for Al-3-B. The difference between Al-B and Al-3-B is 0.02%IACS, and can be considered equal. The conductivity difference between the grain refiners is not substantial, where the largest difference to be observed is between Al-3-D and Al-1-D which is of below 1.5%IACS. This difference is also likely influenced by the large volume of pores in Al-3-D compared to Al-1-D.

Figure 49 show the measured conductivity value for every AlSi7 sample type and are plotted with increasing conductivity from left to right Figure

Figure 49: Conductivity measurements for AlSi7.

For both Al and AlSi7, the samples without grain refiner have the lowest conductivity for A samples and second lowest for B samples. However Al-C and Al-D have the lowest conductivity of its sample type, whereas AlSi7-C and AlSi7-D have the highest conductivity of its sample type. Without adding grain refiner, AlSi7 forms much smaller grains compared to Al. This difference in grain size is largest for C and D samples, which have the lowest solidification rate. A likely reason for why AlSi7-C and AlSi7-D have the highest conductivity is because they have small enough grains to dilute the impurities precipitating at the grain boundaries, while also not having artificial contamination added from the grain refiners. This would also explain why the AlSi7 EMC samples all have a lower conductivity than the most comparable non-EMC AlSi7-D sample. The EMC process increased the volume of pores in the samples and did not decrease the grain size as much for AlSi7 samples compared to Al samples.

From Figure 48 and 49 it can be observed that the conductivity measurements of A, B, and C samples are not of substantial difference and the highest for both alloys, although they are much closer for AlSi7. Therefore, no conductivity trend between grain refiners for these sample types could be found. The differences in measured conductivity for a considerable amount of these samples, is so small that they are likely to be influenced by the calibration drift of the conductivity measurement meter. The D and EMC samples have a larger difference in measured conductivity, and show promising results for further research into grain refinement by EM fields.

Figure 50 shows grain size from the grain analysis algorithm plotted against the conductivity measurements for the Al samples. The coefficient of determination (R^2 value) for the power regression is 0.788. This entails a moderate correlation between conductivity and grain size for Al. It is assumed that conductivity increases as a function of grain size because the volume of grain boundaries increases with decreasing grain size. This is also why a power regression model is used, as grain size is then likely to affect conductivity with a ratio to the power of something.

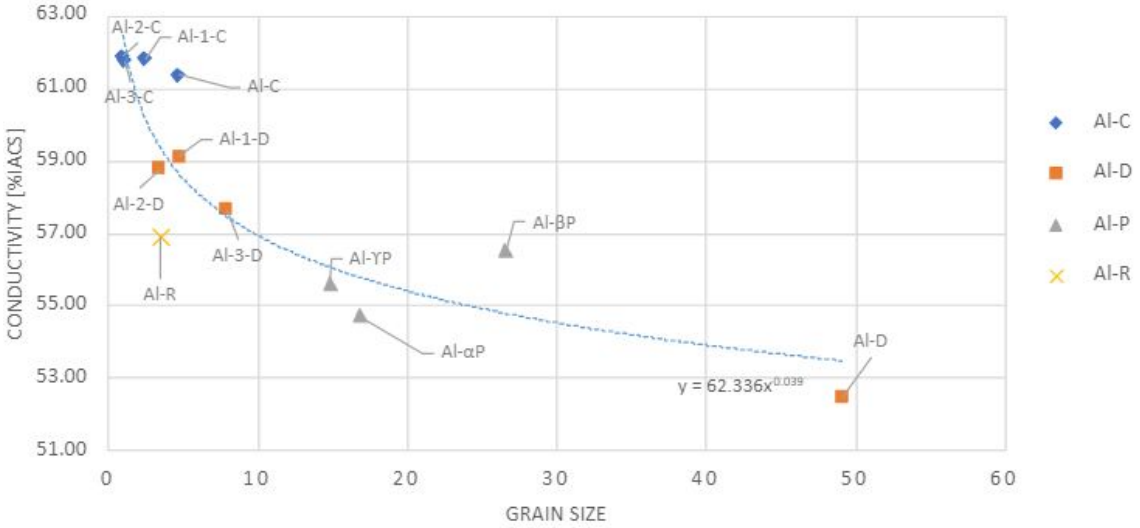

Figure 50: Correlation between conductivity and grain size for Al.

These results indicate an inverse correlation between grain size and conductivity, even when grain refiner is added. The decrease in grain size causes an increase in grain boundaries, which in turn creates a larger area for conductivity reducing precipitates to be distributed over. This explains why a decrease in grain size yields a greater conductivity.

The conductivity values and grain size for AlSi7 was also plotted as seen in Figure 51. With a R^2 value of 0.398, AlSi7 presents with a weak to no correlation.

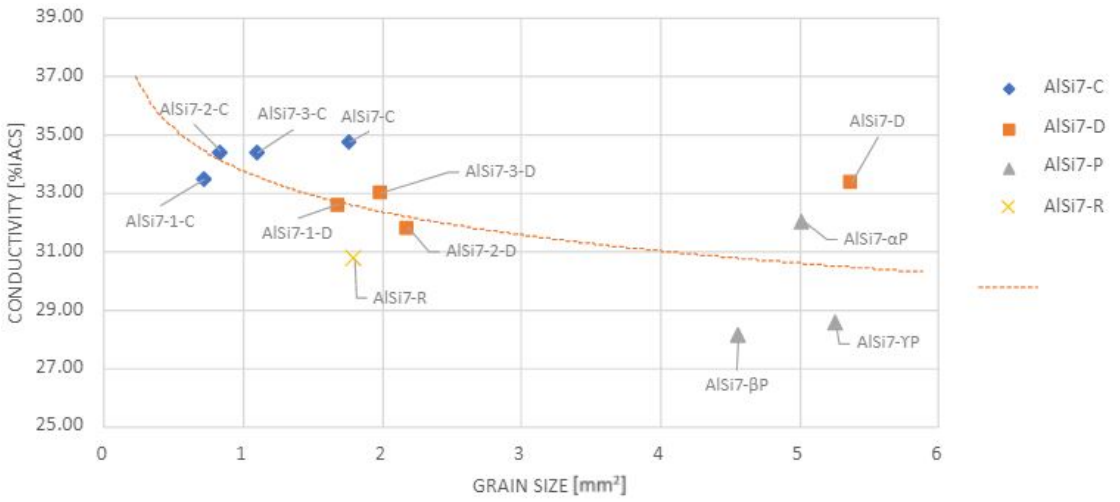

Figure 51: Relationship between conductivity and grain size for AlSi7.

There are two likely factors explaining the low coefficient of determination. First, the small sample size means that small variations may have detrimental effects on the comparison. Second, the AlSi7 samples had noticeably more defects than the Al samples, which may have influenced both the digital processing and the conductivity meter. Defects, such as scratches from polishing and pores, distorted the results from the grain counting algorithm causing inaccuracies in the results. Samples with more defects were also found to have a lower conductivity measurement than expected.

Both of these correlation plots show how the different sample types tend to group up, except for Al-D and AlSi7-D. If the grain analysis algorithm could accurately determine the grain size for A and B samples and added to the plots, it is likely that they could show similar grouping. Overall the A and B samples also have both the smallest grain size and highest conductivity compared to other sample types, indicating that they could follow the same trends seen in these plots.

5 Conclusion

This thesis studied the effect of grain refiners and EM fields on the evolution of the grain structure and conductivity of aluminium and its alloys. The following conclusions have been drawn from the course of subject work:

Effect of solidification rate and the addition of grain refiners:
1. In all regularly cast samples, including those with grain refiner, slower solidification resulted in larger grains.
2. For the Al samples, excluding the RSD samples, these grains converged to varying extent towards the center of the sample. However, the AlSi7 samples showed a more uniform distribution of grains without any convergence.
3. The addition of grain refiner caused a substantial reduction of grain size in most samples. The effect of the grain refiner was clear in all Al tests. In the AlSi7 samples the grains were already so small that the grain refiners effect was substantially lowered.
4. However, the grain refiner does not seem to affect the convergence towards the center in the Al samples, nor the uniform, scattered pattern of the AlSi7 samples.
5. The particles in the grain refiner agglomerates when in the liquid aluminium,thereby decreasing the efficiency of the grain refiner.

Effect of EM fields:
1. Applying an EM field to the samples during solidification caused a significant increase in sample porosity, but it also had a significant effect on the microstructure.
2. All EM samples experienced an increase in the number of pores and defects from their non-EM counterparts. However, this effect was not as prominent in the pancake coil samples as in the round coil samples.
3. The EM field also hampered the grains convergence towards the center of the sample, as in contrast to the non-EM Al samples. This caused the Al samples to have a more similar microstructure to the AlSi7 samples.
4. The pancake coil Al samples showed a noticeable reduction in grain size, though the samples were not enough to determine if the reduction in size had a linear correlation with EM field strength. The reduction effect on grain size was not noticeable in the AlSi7 pancake coil samples, likely because the mushy zone in AlSi7 slows the movement from the EM stirring.
5. For all samples generated by using the round coil with the strongest EM field, the reduction in grain size was prominent, yielding a reduction that could compete with addition of grain refiners.

Effect on conductivity:
The conductivity for AlSi7 was as expected substantially lower than that of Al, however the effect from EM field samples was likely affected by the porosity of the samples. Pure Al conducts electricity best without the addition of alloying elements, and the reduction in conductivity for Al compared to AlSi7 is expected.
1. The effect of grain refiner seems to be negligible in comparison to the effect of surface defects.
2. The EM samples had a substantially lower conductivity than the rest of the samples, though this is likely to be substantially affected by the amount of surface defects in these samples.
3. Our results indicate a inverse correlation between grain size and conductivity, even when grain refiners are added.

Final remark:
The solidification time, the addition of grain refiner and the application of an EM field have substantial effects on the microstructure of the aluminium. This report provides a base for further knowledge to be built upon. The most prominent areas for further exploration includes optimising the application of EM fields, how to reduce porosity in EM casts and how to accomplish this at a larger scale. Further research in these areas would make industrial application a possibility, possibly even eliminating the need for grain refiners.

6 Future Research and Outlook

This work is a pioneer research into the effect of grain refiners, solidification speed, and EM fields on the evolution of the microstructure of aluminium and its alloys. The results observed during this work builds a foundation for further research into electromagnetic grain refinement and provides a baseline for comparing this with commercial grain refiners. The most important factors to explore further are likely to be:

1. EM field strengths
2. varying the frequency of the EM field
3. the effect of grain refiners in comparison to EMC and effects of degassing

Before moving on to large scale testing, the EM field investigation should be optimized. This thesis only investigates the effect of two different coil types with varying field strengths of 2.20 mT, 4.20 mT, 6.04 mT delivered by a parallel pancake coil arrangement and 158.56 mT delivered by a double round coil. The optimal EM field strength can be determined by expanding the range and adding more intervals of testing. By establishing enough data-points, an accurate model of the effect EM fields have on castings could be developed.

All samples EMC samples in this study utilised 50Hz AC power and it is likely that changing the frequency could substantially increase the grain refinement effect. This is because lower frequencies penetrate deeper into the molten metal. It is also possible to tune the frequency to match the resonance frequency of the aluminium in the mould to further increase the effect of the EM field. The most important part of further research would be to have more samples of each type. The average effect and variance of each field should be investigated on a small scale, before moving on to large scale testing if the results are promising.

The main use of EM casting would likely be as a substitute for grain refiners in materials where purity is important. One such example is the use of pure aluminium in high-voltage transmission lines, where a reduction in aluminium purity would reduce conductivity and hereby the electrical losses. Therefore, further comparisons between grain refiner and EMC for more specified applications would be beneficial.

Several results were affected by the amount of pores in the samples. These pores, as discussed, are likely hydrogen from moisture in the air. By degassing the melt prior casting the pores could be reduced. For future research in this field, all cast samples should be degassed to achieve results that are less affected by pores.

Bibliography

[1] V. Metan, K. Eigenfeld, D. Räbiger, M. Leonhardt, and Eckert S. Grain size control in al–si alloys by grain refinement and electromagnetic stirring. *Journal of Alloys and Compounds*, 2009.

[2] Ch. Vives. Effects of electromagnetic vibrations on the microstructure of continuously cast aluminum alloys. *Advances in Materials Science and Engineering*, 1993.

[3] M. Hassanabadi, S. Akhtar, L. Arnberg, and R. Aune. Grain refinement of commercial ec grade 1370 aluminium alloy for electrical applications. *JOM: The Member Journal of TMS*, 2018.

[4] Granta Design Limited CES EduPack software. Level 3, material universe, 2009.

[5] W. Ebhota and T. Jen. *Intermetallic Compunds*. IntechOpen, 2018. URL https://www.intechopen.com/chapters/58937.

[6] P. Biswas, S. Patra, and M. Mondal. Structure-property correlation of eutectic al-12.4 si alloys with and without zirconium (zr) addition. *International Journal of Cast Metals Research*, 33: 1–12, 05 2020. doi: 10.1080/13640461.2020.1769319.

[7] Anonymous. *Copper wire tables*. Washington Govt. Print. Off, 1991.

[8] T. Kuphaldt. Lessons in electric circuits, 1999. URL https://www.allaboutcircuits.com/textbook/.

[9] W. Callister Jr. and D. Rethwisch. *Materials Science and Engineering*. Wiley, 2011.

[10] The Editors of Encyclopaedia Britannica. magnetic permeability, 2020. URL https://www.britannica.com/science/magnetic-permeability.

[11] Anonymous. Electromagnetism, 2020. URL https://www.electronics-tutorials.ws/electromagnetism/electromagnetism.html.

[12] Kuphaldt. Crest foundation electrical engineering: Dc electric circuits: Inductors, 2002. URL https://learn.lboro.ac.uk/pluginfile.php/504345/mod_resource/content/1/FB-DC7.pdf.

[13] A. Robbins and W. Miller. *Circuit Analysis: Theory and Practice*. Cengage Learning India, 2013. URL http://www.nhu.edu.tw/~chun/BE-Ch13-Inductance%20&%20Inductors.pdf.

[14] Anonymous. Basic facts about inductors [lesson 1] overview of inductors - how do inductors work?, 2010. URL https://article.murata.com/en-us/article/basic-facts-about-inductors-lesson-1.

[15] Anonymous. Ampere's law, 2012. URL https://www.maxwells-equations.com/ampere/amperes-law.php.

[16] Anonymous. Faraday's laws of electromagnetic induction: First & second law, 2021. URL https://www.electrical4u.com/faraday-law-of-electromagnetic-induction/.

[17] G. Wang, M. Dargusch, M. Easton, and D. StJohn. *Chapter 9 - Treatment by External Fields*. Woodhead Publishing Series in Metals and Surface Engineering. Woodhead Publishing, 2018. ISBN 978-0-08-102063-0. doi: https://doi.org/10.1016/B978-0-08-102063-0.00009-6. URL https://www.sciencedirect.com/science/article/pii/B9780081020630000096.

[18] The Editors of Encyclopaedia Britannica. Lorentz force. *Encyclopedia Britannica*, 05 2020. URL https://www.britannica.com/science/Lorentz-force.

[19] The Editors of Encyclopaedia Britannica. magnetic permeability, 2008. URL https://www.britannica.com/science/skin-effect.

[20] W. Middleton and M. Valkenburg. 6 - fundamentals of networks. In W. Middleton and M. Valkenburg, editors, *Reference Data for Engineers (Ninth Edition)*, pages 6–1–6–22. Newnes, Woburn, ninth edition edition, 2002. ISBN 978-0-7506-7291-7. doi: https://doi.org/10.1016/B978-075067291-7/50008-X. URL https://www.sciencedirect.com/science/article/pii/B978075067291750008X.

[21] M. Tangstad. *Metal production in Norway*. akademika, 2013.

[22] K. Soekrisno. The effect of solidification rate on morphology microstructures and mechanical properties of 80%cu-20%sn bronze alloys. *Material science research India*, 03 2010. URL http://www.materialsciencejournal.org/vol7no1/the-effect-of-solidification-rate-on-morphology-microstructures-and-mechanical-properties-of-80cu-20sn-bronze-alloys

[23] Anonymous. Understanding solidification and nucleation in aluminium alloys, 2020. URL https://www.elementum3d.com/white-papers/understanding-solidification-and-nucleation-in-aluminum-alloys/.

[24] D. Askeland and W. Wright. *Essentials of Materials Science and Engineering*. CENGAGE, 2009.

[25] P. Foteinopoulos, A. Papacharalampopoulos, and P. Stavropoulos. On thermal modeling of additive manufacturing processes. *CIRP Journal of Manufacturing Science and Technology*, 20, 10 2017. doi: 10.1016/j.cirpj.2017.09.007.

[26] J. Campbell. *Castings*. Butterworth-Heinemann, 1991.

[27] S. Hasse. Microporosity, 2022. URL https://www.giessereilexikon.com/en/foundry-lexicon/Encyclopedia/show/microporosity-3953/?cHash=50d93a92228e8d59ce93cd72e9ee42df.

[28] S. Hasse. Hydrogen solubility, 2022. URL https://www.giessereilexikon.com/en/foundry-lexicon/Encyclopedia/show/hydrogen-solubility-4337/?cHash=3fb33cdb55421809434093391179007b.

[29] S. Hasse. Hydrogen porosity, 2022. URL https://www.giessereilexikon.com/en/foundry-lexicon/Encyclopedia/show/hydrogen-porosity-4153/?cHash=d06eff4f9ea7076af9f2442f9c668e6b.

[30] J. Campbell. *Castings*. Butterworth-Heinemann, 1991.

[31] J. Anson and J. Gruzleski. The quantitative discrimination between shrinkage and gas microporosity in cast aluminum alloys using spatial data analysis. *Materials Characterization*, 43(5):319–335, 1999. doi: https://doi.org/10.1016/S1044-5803(99)00059-5. URL https://www.sciencedirect.com/science/article/pii/S1044580399000595.

[32] S. Hasse. Rotary degassing, 2022. URL https://www.giessereilexikon.com/en/foundry-lexicon/Encyclopedia/show/rotary-degassing-4427/?cHash=5929b71f8da1b49a764755bc88f710cb.

[33] Dendritic growth, 2022. URL https://www.doitpoms.ac.uk/tlplib/solidification_alloys/dendritic.php.

[34] G. Voort. Metallographic procedures for precious metals, 2012. URL https://vacaero.com/information-resources/metallography-with-george-vander-voort/1251-metallographic-procedures-for-precious-metals.html.

[35] R. Brandt and G. Neuer. Electrical resistivity and thermal conductivity of pure aluminum and aluminum alloys up to and above the melting temperature. *International Journal of Thermophysics*, 10 2007.

[36] P. Desai and C. Ho. Electrical resistivity of aluminum and manganese. *Center for Information and Numerical Data Analysis and Synthesis*, 1984.

[37] Anonymous. Grain refiner, 2020. URL https://www.gallorini.it/2020/12/grainrefiners/.

[38] A. Samuel, S. Mohamed, H. Doty, S. Valtierra, and F. Samuel. Effect of melt temperature on the effectiveness of the grain refining in al-si castings. *Advances in Materials Science and Engineering*, 2018.

[39] H. Safaie, M. Coleman, R. Johnston, A. Das, J. Russell, and C. Pleydell-Pearce. Circular polarized light microscopy to investigate the crystal orientation of aluminium. *Materials Characterization*, 185:111749, 2022. ISSN 1044-5803. doi: https://doi.org/10.1016/j.matchar.2022.111749. URL https://www.sciencedirect.com/science/article/pii/S1044580322000316.

[40] B. Wielage, G. Alisch, T. Lampke, and D. Nickel. *Anodizing–a key for surface treatment of aluminium*, volume 384. Trans Tech Publications, 2008.

[41] S. Swapp. Scanning electron microscopy(sem). *Geochemical Instrumentation and Analysis*, 05 2017. URL https://serc.carleton.edu/research_education/geochemsheets/techniques/SEM.html.

[42] Abdel Salam Hamdy Makhlouf and Mahmood Aliofkhazraei, editors. *Handbook of Materials Failure Analysis with Case Studies from the Aerospace and Automotive Industries*. Butterworth-Heinemann, 2016. ISBN 978-0-12-800950-5. doi: https://doi.org/10.1016/B978-0-12-800950-5.09997-X. URL https://www.sciencedirect.com/science/article/pii/B978012800950509997X.

[43] Anonymous. Does temperature affect conductivity?, 2021. URL https://atlas-scientific.com/blog/does-temperature-affect-conductivity/.

[44] Comsol multiphysics® v. 5.5 (build 359), 2020. URL www.comsol.com.

Appendix

A Dimensions of Casting Moulds

Table 5: Dimensions of the casting moulds in mm.

Dimensions [mm]	Cylindrical iron mould	RSD iron mould	Graphite mould	Insulation	Insulation lid
Total diameter	98		50	82	82
Inner diameter	40	40	30	55	
Total height	102	39	50	75	25
Inner height	52	12	40	50	
Width		64			
Length		76			

B Magnetic Field Measurements

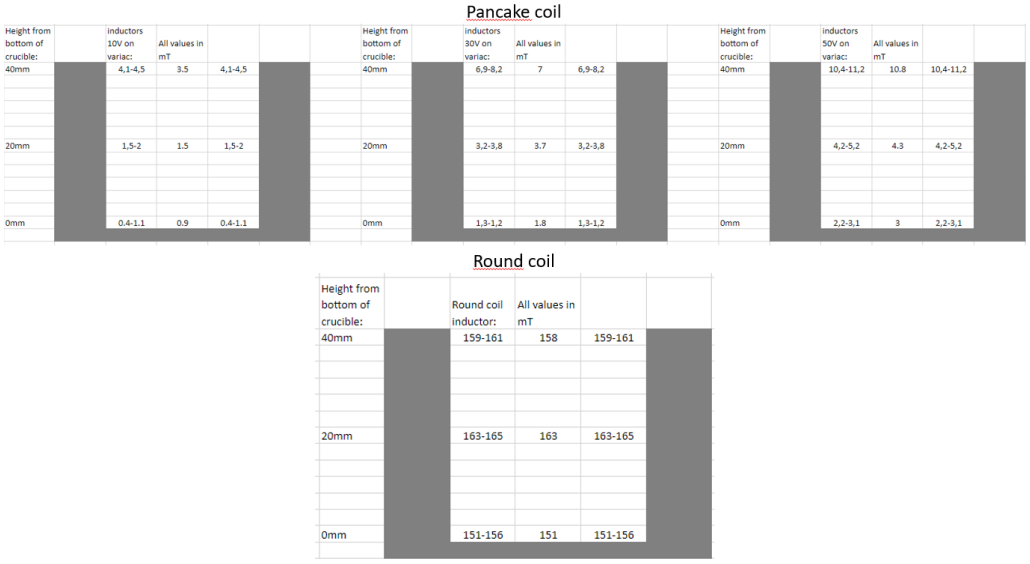

Figure 52: Measurements of field strength in the mold for the strength used.

C Dimensions of the Electromagnetic Coils

Table 6: Dimensions of the electromagnetic coils in mm.

Dimensions [mm]	Round coil	Pancake coil top	Pancake coil bottom
Diameter	130	230	160
Height			150

D Grain Size Data

Sample	Average grain size [mm]		Sample	Average grain size [mm]
Al-C	4.685154435		AlSi7-C	1.757799611
Al-1-C	2.44988258		AlSi7-1-C	0.725809177
Al-2-C	0.956123957		AlSi7-2-C	0.83927925
Al-3-C	1.059089375		AlSi7-3-C	1.102562114
Al-D	49.0722814		AlSi7-D	5.377222395
Al-1-D	4.728817265		AlSi7-1-D	1.686547666
Al-2-D	3.400480992		AlSi7-2-D	2.180361119
Al-3-D	7.924219227		AlSi7-3-D	1.985557779
Al-αP	16.78788574		AlSi7-αP	5.022541509
Al-βP	26.58081909		AlSi7-βP	4.560354949
Al-ϒP	14.83580601		AlSi7-ϒP	5.263486184
Al-R	3.494540874		AlSi7-R	1.803792897

Figure 53: Grain size data for all circular Al and AlSi7, C and D samples.

E Conductivity Measurements

Label	Linear approach to conductivity	Avg conductivity	egde1 of sample	middle of sample	egde2 of sample	Alloy	Grainrefiner
Al-A	61.37	61.37	61.50	61.30	61.30	Al99.7	
Al-B	61.86	61.93	61.90	62.10	61.80	Al99.7	
Al-C	61.39	61.53	61.60	61.50	61.50	Al99.7	
Al-CX	61.62	61.83	61.80	61.90	61.80	Al99.7	
Al-D	52.47	52.70	51.70	51.00	55.40	Al99.7	
Al-DX	57.80	58.10	58.80	57.10	58.40	Al99.7	
Al-R	56.91	57.23	59.90	53.50	58.30	Al99.7	
Al-RX	54.23	54.57	54.60	49.30	59.80	Al99.7	
Al-1-A	61.92	61.93	61.90	62.00	61.90	Al99.7	KBM
Al-1-B	62.04	62.13	62.00	62.40	62.00	Al99.7	KBM
Al-1-C	61.81	61.97	61.90	62.00	62.00	Al99.7	KBM
Al-1-D	59.12	59.37	60.10	58.30	59.70	Al99.7	KBM
Al-2-A	62.00	62.03	62.00	62.10	62.00	Al99.7	GR 3:1
Al-2-B	61.96	62.07	62.00	62.10	62.10	Al99.7	GR 3:1
Al-2-C	61.89	62.07	62.00	62.10	62.10	Al99.7	GR 3:1
Al-2-D	58.80	59.07	59.50	58.30	59.40	Al99.7	GR 3:1
Al-αP	54.74	55.10	52.90	54.30	58.10	Al99.7	
Al-3-A	61.71	61.77	61.80	61.80	61.70	Al99.7	Aleastur 5:1
Al-3-B	61.84	61.97	62.00	62.00	61.90	Al99.7	Aleastur 5:1
Al-3-C	61.77	61.97	61.90	62.10	61.90	Al99.7	Aleastur 5:1
Al-3-D	57.65	57.93	60.20	57.30	56.30	Al99.7	Aleastur 5:1
Al-αPX	56.32	56.73	57.90	53.90	58.40	Al99.7	
Al-βP	56.56	56.93	57.90	54.00	58.90	Al99.7	
Al-βPX	59.70	60.13	60.40	60.00	60.00	Al99.7	
Al-γP	55.61	56.00	54.80	55.50	57.70	Al99.7	
Al-γPX	57.55	58.00	59.20	59.30	55.50	Al99.7	
AlSi7-αP	32.08	32.23	33.20	31.50	32.00	AlSi7	
AlSi7-αPX	30.32	30.50	30.50	29.40	31.60	AlSi7	
AlSi7-βP	28.17	28.33	28.00	25.50	31.50	AlSi7	
AlSi7-R	30.76	30.90	32.70	28.70	31.30	AlSi7	
AlSi7-βPX	27.25	27.43	29.40	21.00	31.90	AlSi7	
AlSi7-RX	30.52	30.67	32.80	31.10	28.10	AlSi7	
AlSi7-γP	28.60	28.77	29.70	25.00	31.60	AlSi7	
AlSi7-γPX	30.34	30.53	29.50	30.70	31.40	AlSi7	
AlSi7-2-A	34.13	34.13	34.30	34.00	34.10	AlSi7	GR 3:1
AlSi7-2-B	33.80	33.83	34.00	33.70	33.80	AlSi7	GR 3:1
AlSi7-2-C	34.44	34.50	34.60	34.50	34.40	AlSi7	GR 3:1
AlSi7-2-D	31.83	31.93	32.60	31.00	32.20	AlSi7	GR 3:1
AlSi7-A	34.03	34.03	34.00	33.70	34.40	AlSi7	
AlSi7-B	34.23	34.27	34.70	34.10	34.00	AlSi7	
AlSi7-C	34.76	34.83	34.80	34.80	34.90	AlSi7	
AlSi7-CX	33.51	33.60	32.50	34.20	34.10	AlSi7	
AlSi7-D	33.39	33.50	33.20	34.20	33.10	AlSi7	
AlSi7-DX	32.37	32.50	32.40	33.00	32.10	AlSi7	
AlSi7-1-A	34.12	34.13	34.60	33.80	34.00	AlSi7	KBM
AlSi7-1-B	34.89	34.93	35.00	34.60	35.20	AlSi7	KBM
AlSi7-1-C	33.52	33.60	33.60	33.40	33.80	AlSi7	KBM
AlSi7-1-D	32.62	32.73	33.70	32.20	32.30	AlSi7	KBM
AlSi7-3-A	34.78	34.80	35.10	34.10	35.20	AlSi7	Aleastur 5:1
AlSi7-3-B	34.48	34.53	34.60	34.30	34.70	AlSi7	Aleastur 5:1
AlSi7-3-C	34.42	34.50	34.50	34.60	34.40	AlSi7	Aleastur 5:1
AlSi7-3-D	33.01	33.13	33.60	32.50	33.30	AlSi7	Aleastur 5:1

Figure 54: Conductivity Measurements for all samples.

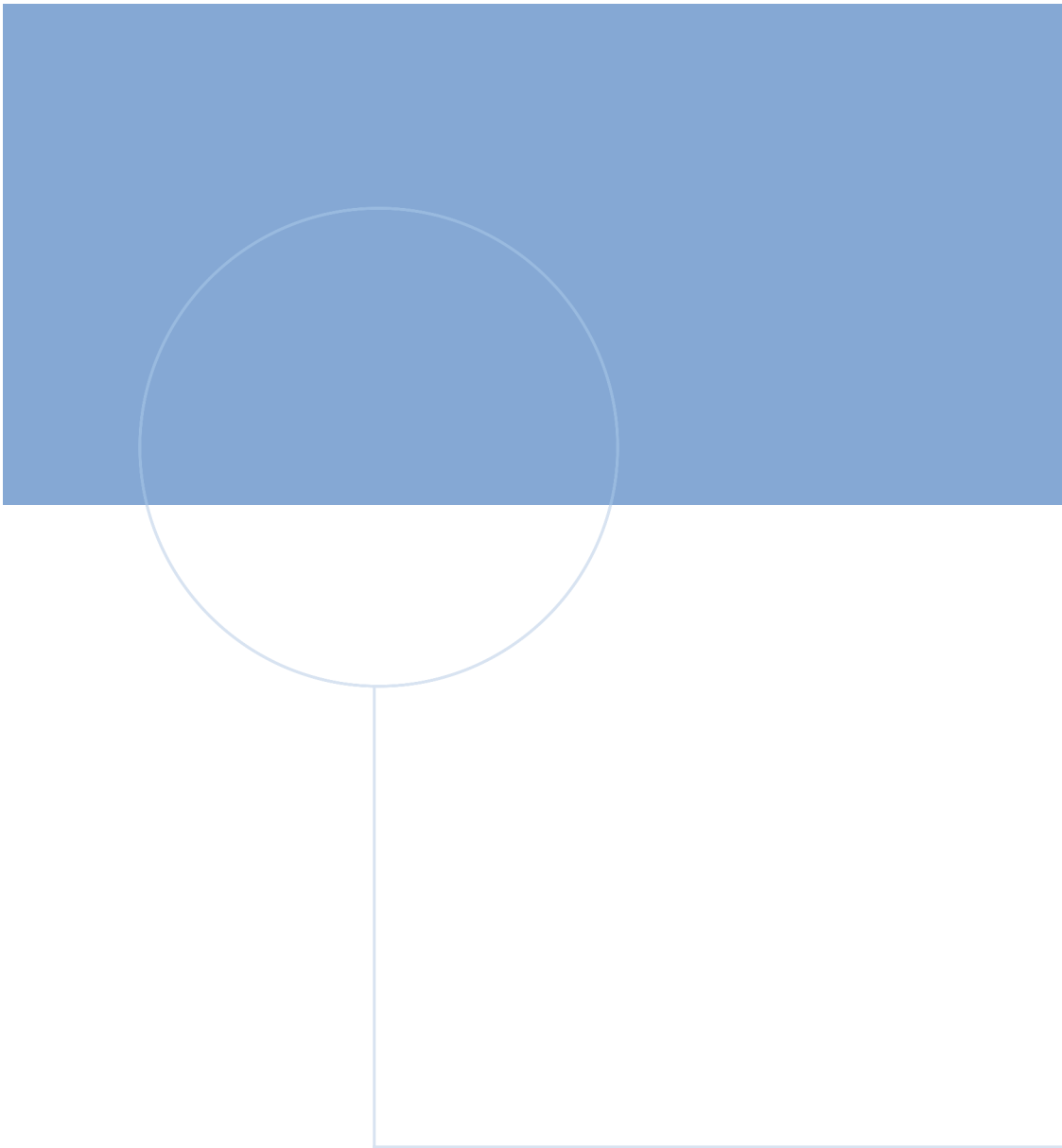

NTNU

Kunnskap for en bedre verden